



**BOUNDARY LAYER CONTROL USING
MICRO-ELECTROMECHANICAL SYSTEMS
(MEMS)**

THESIS

David M. Borgeson, Captain, USAF

AFIT/GSO/ENY/02-1

**DEPARTMENT OF THE AIR FORCE
AIR UNIVERSITY**

AIR FORCE INSTITUTE OF TECHNOLOGY

Wright-Patterson Air Force Base, Ohio

APPROVED FOR PUBLIC RELEASE; DISTRIBUTION UNLIMITED.

Report Documentation Page

Report Date 26 Mar 2002	Report Type Final	Dates Covered (from... to) Sep 2000 - Mar 2002
Title and Subtitle Boundary Layer Control Using Micro-Electromechanical systems (MEMS)	Contract Number	
	Grant Number	
	Program Element Number	
Author(s) Capt David Borgesonk USAF	Project Number	
	Task Number	
	Work Unit Number	
Performing Organization Name(s) and Address(es) Air Force Institute of Technology Graduate School of Engineering and Management (AFIT/EN) 2950 P Street, Bldg 640 WPAFB, OH 45433-7765	Performing Organization Report Number AFIT/GSO/ENY/02-1	
Sponsoring/Monitoring Agency Name(s) and Address(es) Dr. Richard B. Rivir AFRL/PRTT 1950 Fifth Street WPAFB, OH 45433-7251	Sponsor/Monitor's Acronym(s)	
	Sponsor/Monitor's Report Number(s)	
Distribution/Availability Statement Approved for public release, distribution unlimited		
Supplementary Notes The original document contains color images.		
Abstract : This study investigated the use of MEMS based devices to control the boundary layer separation from a circular cylinder in cross flow. Velocity profiles were measured experimentally in a low speed wind tunnel. Momentum thickness was measured as the primary way to determine a change in the flow field. The goal was to determine the angular location and frequency of operation that would provide an effect on the boundary layer of the cylinder. A 25% reduction of momentum loss in the cylinder wake was detected with an optimal angle of 69 degrees and an optimal frequency of operation equal to that of the shedding frequency of the cylinder.		
Subject Terms Micro-ElectroMechanical Systems (MEMS), Boundary Layer, Momentum Thickness		
Report Classification unclassified	Classification of this page unclassified	

Classification of Abstract unclassified	Limitation of Abstract UU
Number of Pages 92	

The views expressed in this thesis are those of the author and do not reflect the official policy or position of the United States Air Force, Department of Defense, or the U.S. Government.

AFIT/GSO/ENY/02-1

BOUNDARY LAYER CONTROL USING MICRO-ELECTROMECHANICAL SYSTEMS (MEMS)

THESIS

Presented to the Faculty

Department of Aeronautics and Astronautics

Graduate School of Engineering and Management

Air Force Institute of Technology

Air University

Air Education and Training Command

In Partial Fulfillment of the Requirements for the

Degree of Master of Science

David M. Borgeson, BS

Captain, USAF

March 2002

APPROVED FOR PUBLIC RELEASE; DISTRIBUTION UNLIMITED.

AFIT/GSO/ENY/02-1

BOUNDARY LAYER CONTROL USING MICRO-ELECTROMECHANICAL
SYSTEMS (MEMS)

David M. Borgeson, BS
Captain, USAF

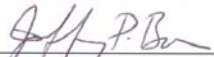
Approved:



Milton E. Franke (Chairman)

13 Mar 2002

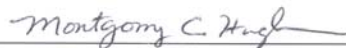
Date



Jeffrey P. Bons (Co-Chairman)

13 Mar 2002

Date



Montgomery Hughson (Member)

13 Mar '02

Date

Acknowledgments

I would like to express my sincere appreciation to my faculty advisors, Dr. Milton Franke and Maj. Jeffrey Bons, for their guidance and support throughout the course of this thesis research. I am greatly appreciative of the support of the technical personnel of AFIT for their efforts to provide supplies and equipment expertise needed along the way.

Thanks must be given to Capt Patrick Wade who consistently provided me with a good sanity check and provided the all-important unbiased audience to discuss test results and theories to ensure they made sense. Sharing research space, he allowed me to interrupt his testing to ensure I was able to gather the data I needed for this research.

David M. Borgeson

Table of Contents

	Page
Approval Page	ii
Acknowledgements	iii
Table of Contents	iv
List of Figures	vi
List of Tables	ix
List of Symbols	x
Abstract	xii
I. Introduction	1
Background	1
Previous Research	1
Research Objective and Scope	3
II. Theory	5
Cylinder Separation	5
Shedding Frequency	9
MEMS Construction	11
MEMS Control of the Boundary Layer	16
Momentum Loss	18
III. Test Hardware	20
Wind Tunnel	20
Instrumentation	23
Data Acquisition System	25
IV. Methodology	27
Angular Location and Coordinate System	27
MEMS Release, Mounting, and Wire-Bonding	29
Testing	36

V.	Data Reduction	41
	Air Density	42
	Bernoulli's Equation	43
	King's Law	44
VI.	Results and Discussion	46
	Boundary Layer Pitot Data	46
	Hot Wire Data	49
	Error Analysis	60
VII.	Conclusions and Recommendations	63
Appendix A.	Data Acquisition/Manipulation	66
Appendix B.	Error Determination	71
References	75
Vita	76

List of Figures

Figure		Page
1.	Pitched and Skewed VGJ's	2
2.	Separation Point of a Boundary Layer Along a Flat Plate	5
3.	Ideal Pressure Streamlines Around a Circular Cylinder	6
4.	Separation on a Cylinder	7
5.	Comparison of Fluid Theory to Experimentation	8
6.	Laminar vs. Turbulent Boundary Layer Separation	9
7.	Measured Strouhal Number for Vortex Shedding for a Cylinder	10
8.	Shedding Visualization for Flow Past a Cylinder	11
9.	MEMS Submitted Design	13
10.	MEMS Tab Deflection	14
11.	Schematic of Single Line of MEMS Devices	14
12.	Electrical Contacts for MEMS	15
13.	MEMS Device Motion	16
14.	Momentum and Displacement Thickness	19
15.	AFIT 12 in. Cross Section Wind Tunnel	20
16.	AFIT 12 in. Cross Section Wind Tunnel Inlet	21
17.	AFIT 12 in. Cross Section Wind Tunnel Exhaust	21
18.	Test Section Dimensions	22
19.	Wake and Boundary Layer Pitot Tubes with Pressure Transducer	23
20.	Standard Boundary Layer Hot Wire	24
21.	IFA – 100 Hot Wire Control Device	25

22.	Arc-Angle of MEMS on Circular Cylinder	27
23.	Angular Location and Coordinate Cross Section	28
24.	(x, y, z) Coordinate System	29
25.	Acetone (ACE) Phase (MEMS Release Process)	31
26.	Timed HF Bath (MEMS Release Process)	32
27.	Released MEMS Devices	34
28.	Theoretical Cross Section of Mounted MEMS Devices	34
29.	Electrical Connections Between Adjacent MEMS Structures	36
30.	Map of Spanwise MEMS Layout on Cylinder	38
31.	Measure of Data Acquisition Points	39
32.	Angle Measuring	40
33.	Digital Barometer	42
34.	Digital Temperature Readout	43
35.	Boundary Layer Pitot Tube Data	47
36.	Static Hot Wire (Determining α Optimal)	49
37.	Static Hot Wire (Determining f Optimal)	50
38.	Hot Wire Probe Data (Wake Profiles)	52
39.	Position of Data Relative to Position of MEMS Devices	54
40.	Frequency Sensitivity Analysis	54
41.	Experimental Shedding Frequency	55
42.	FFT Frequency Signal from Hot Wire Data	56
43.	Sensitivity Analysis to Changes in α	57
44.	Effects of Changing Free Stream Velocity	58

45.	Theoretical Shedding Frequency vs. f_{Optimal}	58
46.	α Optimal at 10 m/s	59
47.	Optimal Frequency f at $\alpha = 69^\circ$	60
48.	Sample Graph of Data used to Obtain Error	62

List of Tables

Table		Page
1.	MEMS Electrical Properties	37
2.	Sample Format of Data	41
3.	Integrated Wake Values (\square_{wake})	53

List of Symbols

<u>Symbol</u>	<u>Definition</u>
ACE	Acetone
AFIT	Air Force Institute of Technology
AFRL/PR	Air Force Research Laboratory Propulsion Directorate
AFRL/SN	Air Force Research Laboratory Sensors Directorate
D	Diameter of Cylinder
DAGSI	Dayton Area Graduate Studies Institute
DC	Direct Current
E	Error
E_{ave}	Precision Error
f	Shedding Frequency
f	Frequency of Operation of MEMS
FFT	Fast Fourier Transform
HF	Hydrofluoric Acid
HW	Hot Wire
I	Current
inHG	inches of Mercury
K	Kelvin
LPT	Low Pressure Turbine
MEMS	Micro-ElectroMechanical Systems

METH	Methanol
MUMPs	Multi-User MEMS Processes
P	Data of Interest (Error Calculation)
P_{mean}	Average Value of Similar Data Sets (Error Calculation)
$P_{\text{stagnation}}$	Stagnation or Total Pressure
P_{static}	Static Pressure
q_w	Heat Transfer
R	Gas Constant
Re_D	Reynolds Number Based on Cylinder Diameter
St	Strouhal Number for Cylinder Vortex Shedding
T	Temperature
U or U_{inf}	Free Stream Velocity
u	Local Velocity
VGJ	Vortex Generator Jet
VI	Virtual Instrument
VPP	Volts Peak-to-Peak
<u>Greek</u>	<u>Definition</u>
θ	Angular Location of MEMS on Cylinder Surface
δ^* or δ_{star}	Displacement Thickness
θ	Momentum Loss Boundary Layer
θ_{wake}	Momentum Loss in Turbulent Wake
μ	Viscosity
ν	Kinematic Viscosity

□

Air Density

□

Arc-Angle

Abstract

This study investigated the use of MEMS devices to control the boundary layer separation from a circular cylinder in cross flow. Measurements were accomplished in AFIT's low-speed, 12-inch cross section wind tunnel. Velocity curves integrated for the momentum thickness were the primary means of detecting changes in the flow field. MEMS placed spanwise across the length of the cylinder were actuated in a variety of operating frequencies and at a variety of angular positions relative to the incoming flow. It was the goal to determine which combination of angle and frequency would best serve the purpose of boundary layer control. An optimal angle of 69 degrees was discovered, and the optimal frequency equal to that of the shedding frequency provided the best solution. Of the tests conducted, these conditions allowed nearly a 25% reduction of momentum loss in the cylinder wake.

BOUNDARY LAYER CONTROL USING MICRO-ELECTROMECHANICAL SYSTEMS (MEMS)

I. Introduction

Background

Of great importance to the turbine designer is the idea of boundary layer separation. Low speed turbines, known as low pressure turbines (LPT), that operate at low Reynolds number (below 95000) have been shown to have considerable losses associated with suction surface separation. Some studies indicate an increase of nearly 300% in loss coefficients at these flow speeds. The main culprit in these losses has been found to be the separation of the boundary layer over the trailing 50% of the suction surface of the blades. This, of course, leads to considerable decreases in stage efficiency. Considerable efforts are being put forward to increase turbine efficiency, even at the cost of penalizing other critical design parameters of an engine. (River, 2000).

In concert with the Air Force Research Laboratory Propulsion Directorate (AFRL/PR) and the Dayton Area Graduate Studies Institute (DAGSI), the use of micro-electromechanical systems (MEMS) based devices to control separation losses, and thereby increase turbine efficiency, is being investigated.

Previous Research

The problem of controlling the separation of the boundary layer is being looked at by many agencies around the world. Each of these has its own unique approach to solve the problem.

Solid vortex generators are static devices such as vanes and winglets used to control flow separation. These devices placed in the flow produce streamwise vortices. These vortices transport freestream momentum across the boundary layer. This causes momentum to be transported into the near wall flow, preventing separation. (Johnston, 1999).

The Vortex Generator Jet (VGJ) is another application into which researchers are looking to solve the problem of boundary layer separation. Steady state and pulsed VGJ's are being studied at this time. VGJ's produce counter rotating vortex pairs that provide the momentum transfer across the boundary layer. By pitching the jets at angles other than normal to the surface (90 degrees) a dominant vortex and a weaker counter-rotating vortex is produced. The momentum transfer from this stronger dominant vs. weak vortex pair may provide more efficient forcing in the boundary layer. (Johnston, 1999). Figure 1 provides the VGJ defining parameters.

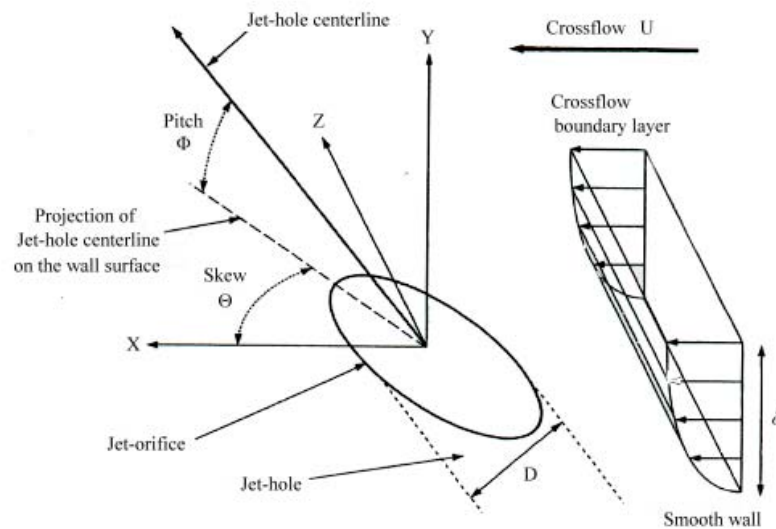


Figure 1. Pitched and Skewed VGJ's. (Khan, 2000).

In 1994, the technique using MEMS devices to create leading-edge vortex control was envisioned. By using vortex flap theory, a differential effect can be used to cause asymmetric loading on the wing of an aircraft. This loading asymmetry can be used to cause moments on all three axes of an aircraft. The intrinsic benefits of using MEMS devices on the scale of microns in size are numerous. Some of which include providing maneuvering capabilities that are better and faster and require less power. Tests using an aluminum delta wing model with small stainless steel strips attached to the leading edge have been successful in causing roll maneuvers in the model. (Huang, 2001).

Research Objectives and Scope

Active control, although more involved than passive techniques, can be considerably more flexible in variable operating conditions. Devices used for active control should be small enough that they produce the desired effect with minimal loss in additional drag.

Much research has been done in the testing of different aerodynamic shapes; not the least of these is the cylinder. These tests have normally been carried out with a high aspect ratio (length to diameter) shape. This approximates an infinite length configuration, ensuring the flow is 2-D in nature.

Because of the desired effects, this test was conducted using a cylinder in cross flow suspended between the side walls of the wind tunnel with a large aspect ratio (L/D) of twelve to one ($12/1$). A Reynolds number of approximately 1.3×10^4 was used to ensure laminar flow to help approximate the laminar flow conditions of a low pressure turbine (LPT) mentioned earlier.

The optimal forcing angular location and frequency of a MEMS device were tested. This thesis contains the results of that separation control study. Chapter II contains the theory that guided the test design. Chapter III discusses the test hardware used to conduct the experiments. Chapter IV will outline the methodology used to conduct the experimental procedures. Chapter V describes the formulas used to gather data. Chapter VI contains a discussion of results obtained in this study. Chapter VII will conclude the research with recommendations for future research.

II. Theory

Cylinder separation

Prandtl first described separation of a two-dimensional, steady boundary layer in his 1904, *Über Flüssigkeitsbewegung Bei Sehr Kleiner Reibung*. Prandtl states that the separation point is completely defined by external conditions. As the boundary layer separates from the surface of the structure in question, it is accompanied by an increase in the size of the rotational flow region, which is a region of re-circulating fluid behind the separation point. When this happens, there are only two options for the flow.

Downstream of the separation point the flow will either pass over the vortex of re-circulating fluid and reattach to the surface or never reattach and form a wake behind the separation point. This latter phenomenon is precisely what happens over the cylinder in question used in this experiment. When a wake is formed, it is generally very large, its size on the order of that of the structure itself. (Gad-el-Hak, 1991).

Figure 2 depicts the above concept as applied to a flat plate.

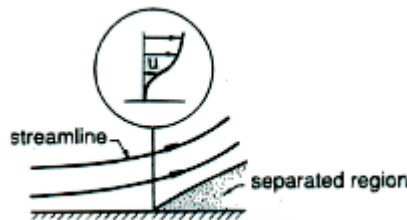


Figure 2. Separation Point of a Boundary Layer Along a Flat Plate. (Gad-el-Hak, 1991).

As flow encounters a favorable pressure gradient, the boundary layer close to the surface will remain attached in a laminar boundary layer. As the flow transitions from a favorable to adverse pressure gradient, then it may separate. The location of separation

for an airfoil depends largely on the incidence angle. For an airfoil at small angle of incidence ($\alpha < 5^\circ$) the boundary layer is small with little to no separation and creates a small wake behind the airfoil. At greater angles however, the boundary layer separates from the suction side of the airfoil and creates a large wake behind the structure. This separation decreases lift and therefore the amount of work that can be done on the fluid by the airfoil. (White, 1991).

For a cylinder the flow is brought to rest at the forward stagnation point at 0 degrees. At this point, pressure is at its maximum. As surface distance (x) is increased, the flow accelerates and the pressure decreases. Hence the flow encounters a favorable pressure gradient at $dp/dx < 0$.

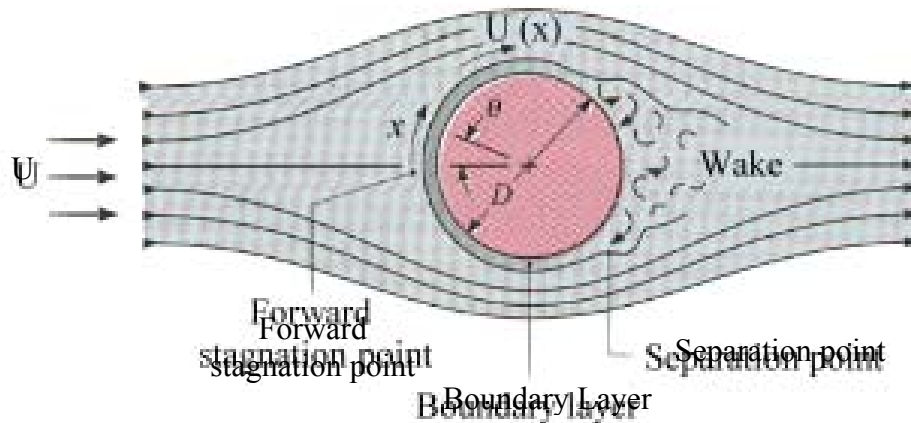


Figure 3. Ideal Pressure Streamlines for a Circular Cylinder. (Incropera, 1996).

For the ideal case, the boundary layer develops due to this favorable pressure gradient where $dp/dx < 0$. The flow reaches a maximum velocity and minimum pressure when $dp/dx = 0$. The flow then decelerates and pressure increases as $dp/dx > 0$. When the velocity gradient at the surface equals zero, the fluid lacks the required momentum to

stay attached, and succumbs to the adverse pressure gradient and separates. This is known as the separation point. Beyond this point, the boundary layer separates from the surface and a wake forms downstream.

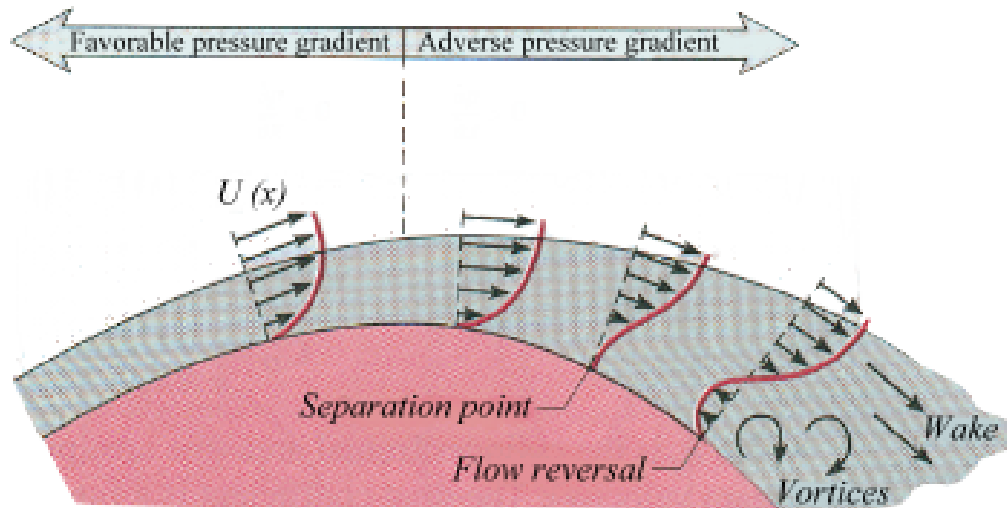


Figure 4. Separation on a Cylinder. (Incropera, 1996).

The previous theoretical discussion is for an ideal case of flow around a cylinder. Of course, real flow does not agree perfectly with theory. The separation point on a cylinder is also dependent on the curvature of the body. Figure 5 compares perfect flow theory to real flow experimental results.

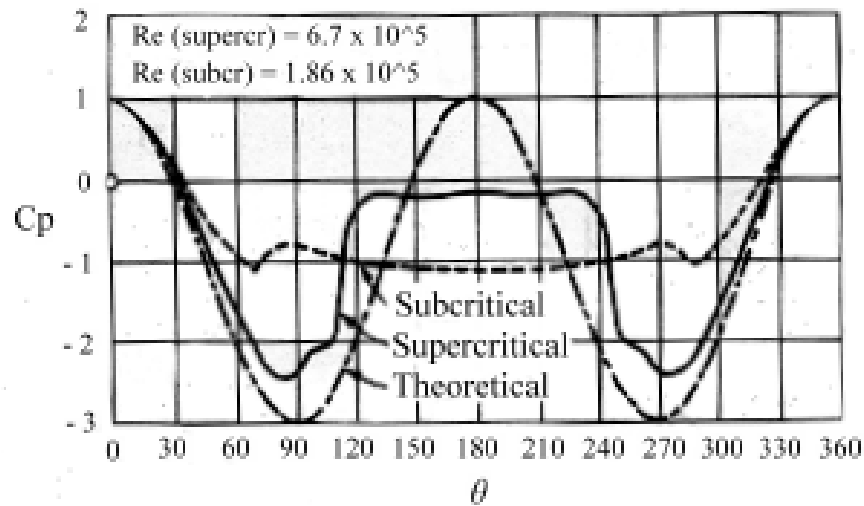


Figure 5. Comparison of Fluid Theory to Experimentation. (White, 1991).

In figure 5, the theoretical curve would separate at the points that velocity is greatest and pressure is smallest and is symmetrical around the cylinder. Experimental data gives another picture. The subcritical plot shows data for laminar flows, and pressure is clearly non-symmetrical around the cylinder. In fact, the flow separates and forms a wake around 70 to 80 degrees and 280 to 290 degrees.

This phenomenon is highly dependent on the Reynolds number which is a function of flow velocity, diameter of the cylinder and fluid property. Because the momentum of a turbulent boundary layer is greater than that of a laminar boundary layer, transition from a laminar to a turbulent boundary layer will delay the separation point. The Reynolds number as a function of diameter is defined by the following equation:

$$Re_D = \frac{\rho U D}{\mu} = \frac{U D}{\nu} \quad (1)$$

Where:

ρ : Air Density (kg/m³)

U:	Free stream velocity	(m/s)
D:	Cylinder diameter	(m)
μ :	Viscosity	(kg/ms)
ν :	Kinematic viscosity	(m ² /s)

The boundary layer remains laminar for $Re_D < 2 \times 10^5$ and the separation point occurs at approximately $\theta = 80^\circ$. For $Re_D > 2 \times 10^5$ the boundary layer will develop a transition region which delays separation to approximately $\theta = 120^\circ$. This is depicted in figure 5. (White, 1991).

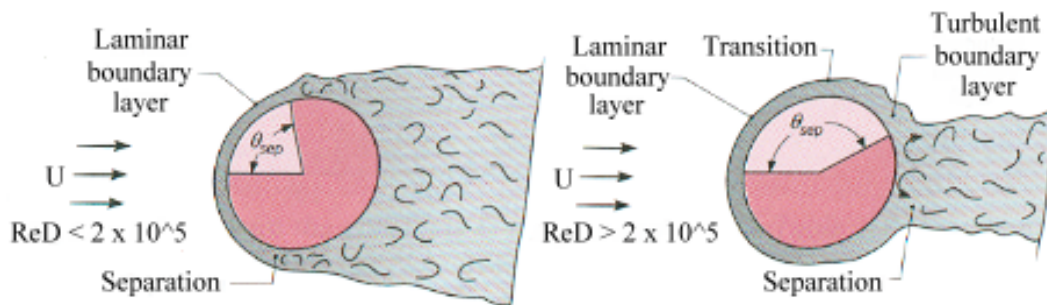


Figure 6. Laminar vs. Turbulent Boundary Layer Separation. (Incropera, 1996).

Shedding Frequency

An interesting phenomenon associated with bluff-body (such as a cylinder) separation is the formation of a large pulsating wake. The pulsating pattern consists of vortex pairs known as Karman vortex streets. (White, 1991).

The frequency at which the vortices shed alternately from the upper and lower surface of a cylinder is known as the shedding frequency. The dimensionless shedding frequency known as the Strouhal number is defined by

$$St = \frac{f D}{U} \quad (2)$$

Where:

f: Shedding frequency of the cylinder (Hz)

D: Cylinder diameter (m)

U: Free stream velocity (m/s)

Figure 7 shows the measured Strouhal number (St) for vortex shedding frequency behind a circular cylinder as a function of Reynolds number. (White, 1991).

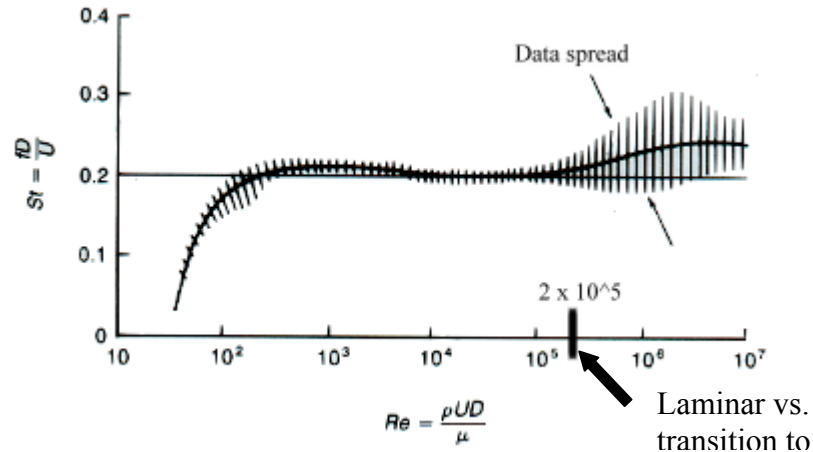


Figure 7. Measured Strouhal Number of Vortex Shedding For a Cylinder. (White, 1991).

For a wide range of Reynolds numbers ($100 < Re < 10^5$) St is equal to approximately 0.2. With the cylinder diameter and the free stream velocity known, the approximate shedding frequency in this Reynolds number range can be found by rearranging Eq (2) to solve for the frequency (f) as

$$f = \frac{0.2 U}{D} \quad (3)$$

The above discussion of vortex shedding frequency is visualized in Figure 8, and proves to be an important parameter in the success of this research.

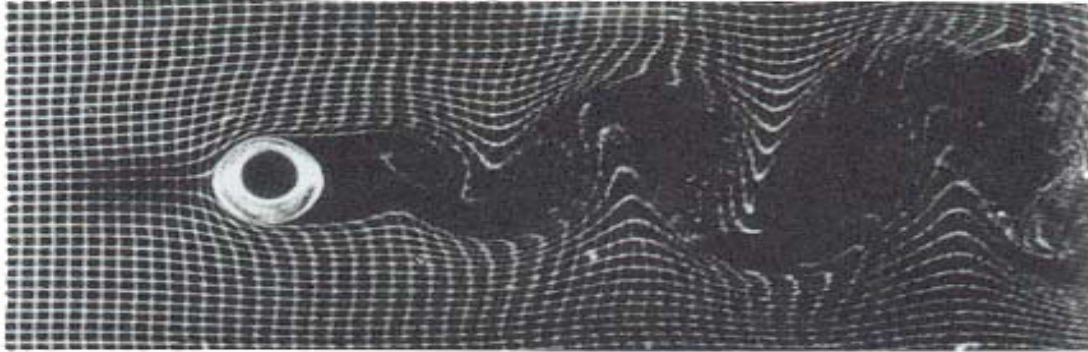


Figure 8. Shedding Visualization for Flow Past a Cylinder. (White, 1991).

MEMS Construction

Micro-ElectroMechanical systems (MEMS) are, as the name implies, small electro-mechanical devices normally measured on the scale of microns (10^{-6}m or μm). They are generally of polysilicon construction with a conducting layer of metal, often gold, applied to the surface in some desired configuration.

Cronos Integrated Microsystems, Inc., using the Multi-User MEMS Processes (MUMPs) commercial program built the MEMS used for this experiment at a cost of \$4,000. The MUMPs process is a three-layer polysilicon surface micromachining process. The following lists of terms are those associated with the design and construction of MEMS devices.

Silicon Substrate: Acts as the base for the entire system. It is $100\ \mu\text{m}$ thick silicon heavily doped with phosphorus to reduce charge feedback to the substrate from the electrostatic devices on top.

Nitride: Approximately 600 nm (10^{-9} m) thick and is deposited on the substrate to act as an electrical isolation layer.

Poly 0: A polysilicon film approximately 500 nm thick and is patterned by photolithography, which is used to separate components in the devices that need to be electrically isolated from one another.

First Oxide: A phosphosilicate glass (PSG) approximately 2 μ m thick which is a sacrificial layer lithographically patterned, removed at the end of the process, and will free the first mechanical layer of polysilicon.

Poly 1: First structural layer of polysilicon deposited with a thickness of 2 μ m and is lithographically patterned with a mask to form the first mechanical structure.

Second Oxide: Lithographically patterned and serves as sacrificial layers just as the first oxide. The pattern allows a mechanical and electrical connection between the Poly 1 and Poly 2 layers.

Poly 2: The second structural layer of polysilicon, deposited at approximately 1.5 μ m thick.

Metal: The metal layer approximately 0.5 μ m provides electrical routing for probing, and bonding.

The release process removes all sacrificial layers and frees the mechanical structures for use. To ensure safety of the structures during shipping, the release process is normally completed by the end user. (Koester, 2001).

The silicon substrate used as the base can measure up to 1 cm². Because the MUMPs design process is a general process for constructing nearly any type of MEMS device, a user purchases a 1 cm² area of "real-estate" on which to design their devices.

The user receives from Cronos Inc. 15 identical copies of the design. For the purpose of this thesis, the substrate measured 10 mm long by 1.25 mm wide. Figure 9 shows the design layout submitted to Cronos Inc.

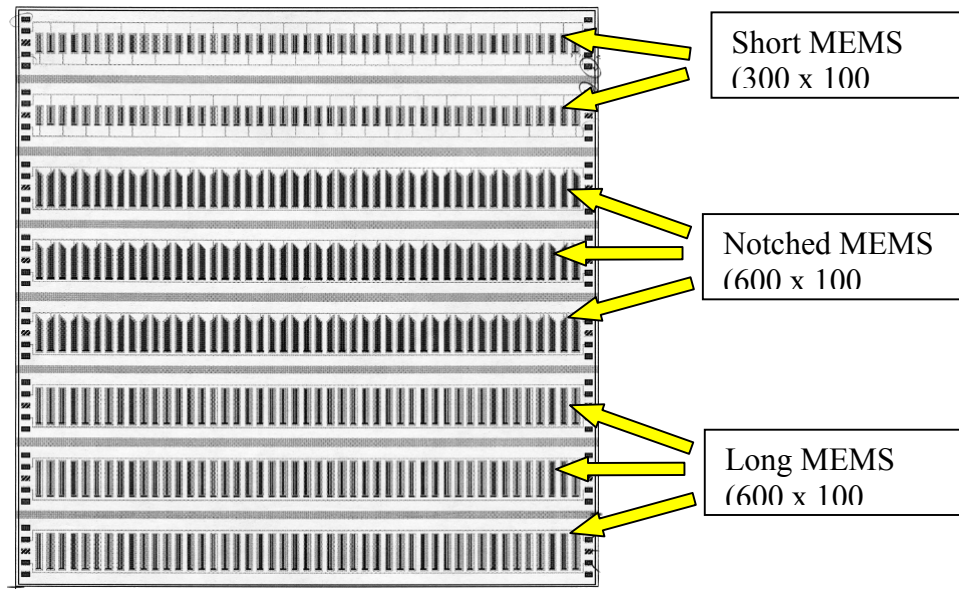


Figure 9. MEMS Submitted Design

In total there were 120 MEMS. There were 30 short MEMS sacrificed for practice in release and mounting runs. Still available are 42 notched MEMS for use in further testing. Used for performance characterization and directly in this experiment was 45 Long MEMS.

Along the bottom of figure 9 are 47 tabs that measure $600\ \mu\text{m}$ long by $100\ \mu\text{m}$ wide. The length to width aspect ratio (length/width) of 6 was designed and the measurements confirmed using a Scanning Electron Microscope (SEM). When released, the process for which will be discussed later, the tabs possess a natural curl from one end to the other causing a cantilever type structure. This is due to the fact that the tabs are

constructed of two dissimilar materials (polysilicon on bottom and gold on top) bonded together. Figure 10 is a SEM picture showing a Long MEMS device on edge to measure max deflection.

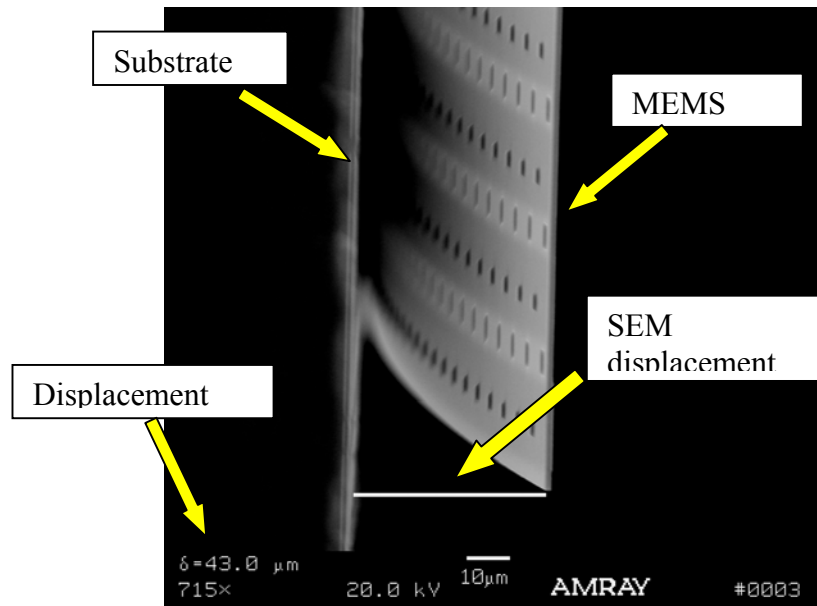


Figure 10. MEMS Tab Deflection

The displacement of the free end measures approximately 43 μm . When a charge is applied across the substrate, the tab is electrostatically attracted to the substrate.

The following diagram gives a view of the MEMS used to perform the boundary layer experiment in question.

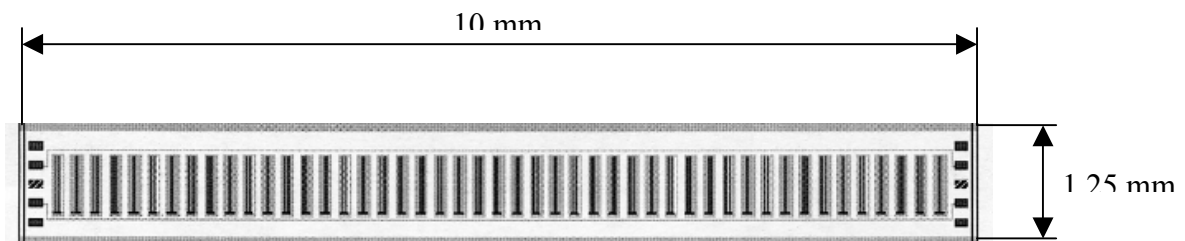


Figure 11. Schematic of Single Line of MEMS Devices

The multi-hued strips in figure 11 represent the MEMS devices. There are 47 "tabs" per 10 mm x 1.25 mm (1 cm x 0.125 cm) length. This test was conducted with 20 MEMS structures daisy chained across the length of a cylinder. This will be discussed in more detail later. Power is provided through the contact pads, seen as dark squares on either end of the structure. Of the five contact pads, the three middle pads are used and the outer two are extras that are not electrically connected. Figure 12 shows a closer view of the contact pad area of the MEMS.

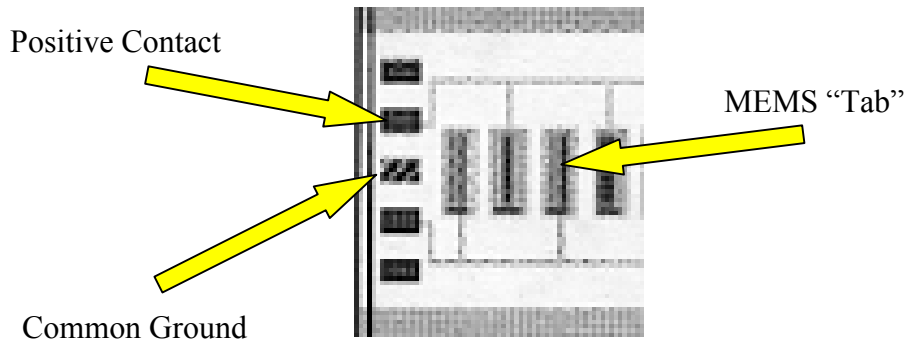


Figure 12. Electrical Contacts for MEMS

The MEMS are wired electrically to every other device in a line. The center pad is the common ground and the two pads next to the negative contact are the positive contacts. For example, the top positive contact provides power to the second and fourth device, while the bottom positive contact provides power to the first and third device shown in figure 12. This electrical connection allows independent actuation of every other device in a line.

MEMS Control of the Boundary Layer

The MEMS produce streamwise vortices through the use of mechanical actuation. This is similar to the vortex generated by the solid static vortex generating devices discussed previously, except that the MEMS have the ability to be actively controlled by electrically actuating them.

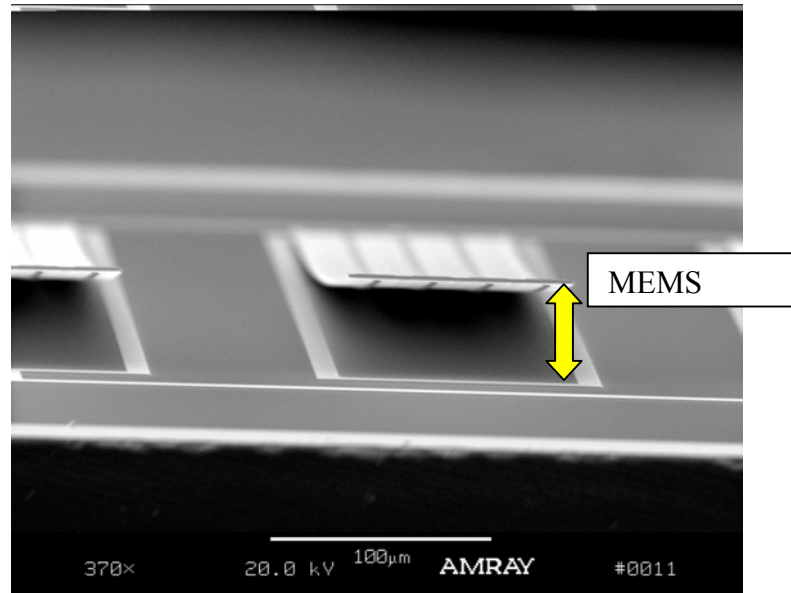


Figure 13. MEMS Device Motion

The theory, which will be laid out in this paper, is one of forcing of fluid into small spanwise vortices that will serve to transport higher momentum fluid down onto the surface of a cylinder in cross flow where lower momentum fluid resides. It is expected that the "energizing" of the boundary layer at the correct angular location and frequency of operation will provide enough momentum to the boundary layer to decrease the momentum loss encountered by the flow as a result of the cylinder in cross flow.

It has been shown that a turbulent boundary layer maintains enough momentum to delay separation from a cylinder in cross flow. With a transition region the boundary layer remains attached to the angle (θ) of approximately 120 degrees. This causes a reduced wake on the trailing edge of a cylinder. The reduced wake size corresponds to reduced momentum loss of the fluid. The less momentum loss encountered by the fluid the less drag on the object in cross flow.

It is known that a turbulent boundary layer can be "artificially" created by a roughening of the surface of the object in cross flow. Through the roughening of the surface, turbulent boundary layers can be created with laminar Reynolds numbers ($Re_D < 2 \times 10^5$). As discussed above, obstructions on the surface cause vortices to form in the streamwise direction. These small vortices create a thin sheet of rotating flow that exchanges the lower momentum of the fluid molecules near the surface with the higher momentum of the fluid molecules above. The higher momentum produces a delay in separation.

Creating roughness on the surface of an airfoil is a passive approach to controlling the separation of the boundary layer. It may not always be desirable to have this technique present on the surface of the airfoil. Therefore an active approach is desired to create the same effect, one that can be turned off and on and even controlled at will to provide the greatest effects. (White, 1991).

As mentioned earlier, fluid that must be provided to the VGJ must be obtained from somewhere. The logical place to find airflow at an appropriate pressure is in the compressor of an engine; meaning flow must be taken from the compressor to the VGJ. This takes mass flow away from the compressor, and adds weight to the engine in the

form of ducting. MEMS on the other hand, in their current state, are lightweight and use relatively little power to drive them. (Khan, 2000).

Momentum loss

Momentum loss represents the energy a fluid must give up in order to traverse around an object in its path. Total gains and losses represent the total momentum loss. The following equation is used to find the momentum loss where " θ " is called the momentum thickness. (White, 1991).

$$\frac{D}{\rho U_{inf}^2} = \theta = \int_0^{\infty} \frac{u}{U_{ing}} \cdot \left(1 - \frac{u}{U_{ing}}\right) dz \quad (4)$$

Momentum thickness calculated using Eq. (4) holds true for any incompressible boundary layer. A second value known as the boundary layer displacement thickness, δ^* , holds for any incompressible flow. As White states, this is simply a statement of "conservation of mass in steady flow". (White, 1991). The equation is seen below.

$$\delta_{star} = \int_0^{\infty} \left(1 - \frac{u}{U_{inf}}\right) dy \quad (5)$$

Figure 14 was constructed using test data and presented in a form to show how θ and δ^* are related.

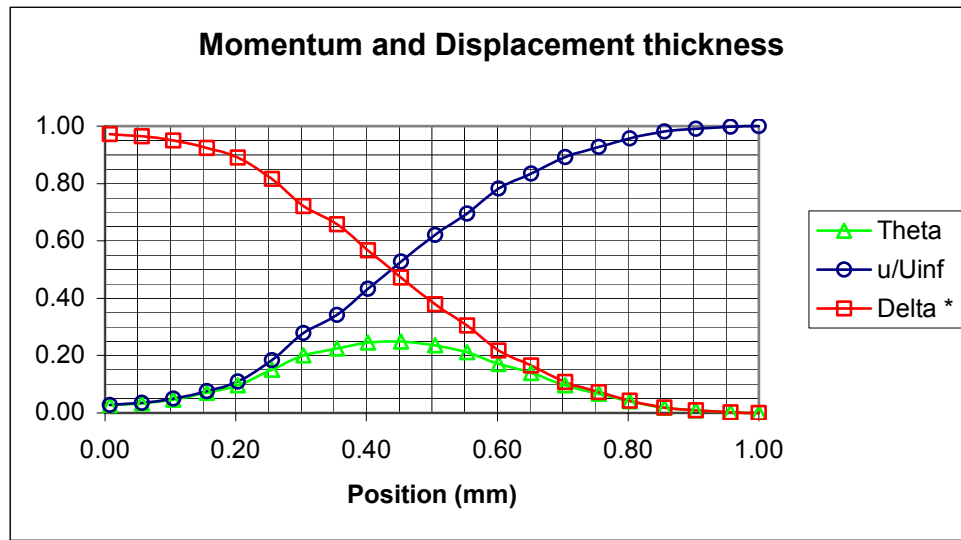


Figure 14. Momentum and Displacement Thickness

When comparing data from a clean cylinder to that of one with the MEMS rotated at some angle (γ) into the flow and actuated with some frequency (f) there should be a considerable difference in the values obtained from Eqs (4) and (5). The primary measure of success will be a decrease in those values. Ideally, there will be a progression toward zero, corresponding to that of no obstruction in the flow. Of course a zero value will never be reached; however, values less than those of the clean cylinder case will prove that the momentum of the fluid has been maintained with less loss due to drag forces.

III. Test Hardware

AFIT 12 Inch (approx. 30 cm) Cross Section Wind Tunnel

All testing was conducted in the AFIT 12 in. (30 cm) cross section Aerodyne wind tunnel (affectionately known to this researcher as the blue monster). The tunnel is located on the AFIT campus in building 640, Rm. 143 (AFIT Aerolab), Wright-Patterson Air Force Base, Ohio. The tunnel configuration allows physical, visual, and instrumentation access to the test section. Constructed mainly of fiberglass, it is an open circuit type wind tunnel. The tunnel is enclosed entirely inside the AFIT Aerolab. As a result, the flow is discharged and mixes with room air before being drawn into the inlet.



Figure 15. AFIT 12 in Cross Section Wind Tunnel

The tunnel inlet consists of a honeycomb structure for smoothing inlet air mounted on the front of the intake bell, as shown in figure 16.

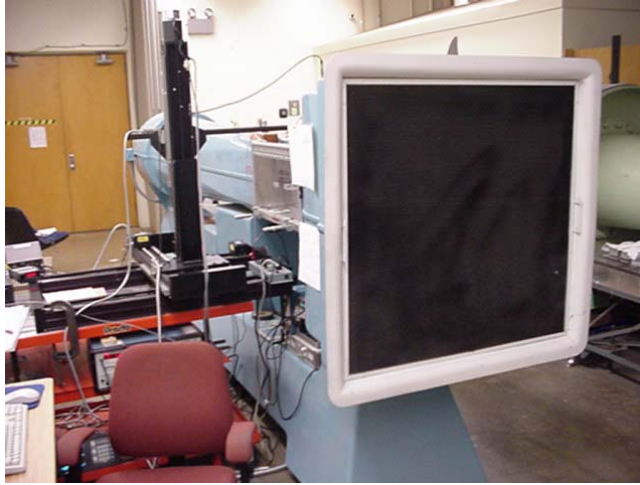


Figure 16. AFIT 12 in Cross Section Wind Tunnel Inlet

A single 25-inch constant area / variable speed fan drives the tunnel. It is controlled by a DC electric motor capable of producing a maximum test section velocity of 63 meters per second (m/s) (140 mi/hr).

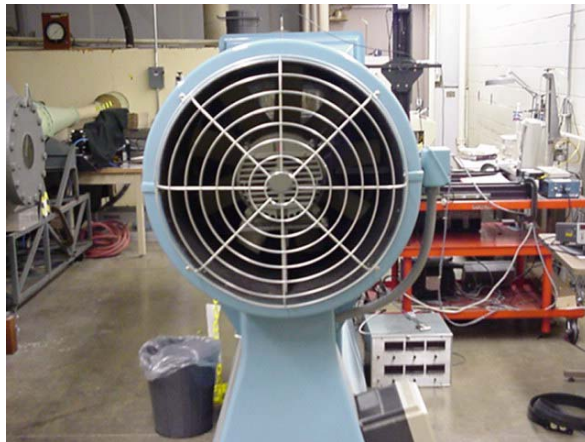


Figure 17. AFIT 12 in Cross Section Wind Tunnel Exhaust

The test section is rectangular in shape measuring 30.5 cm x 30.5 cm x 61 cm (12 in x 12 in x 24 in) for a total volume of 56745 cm³ (3456 in³).

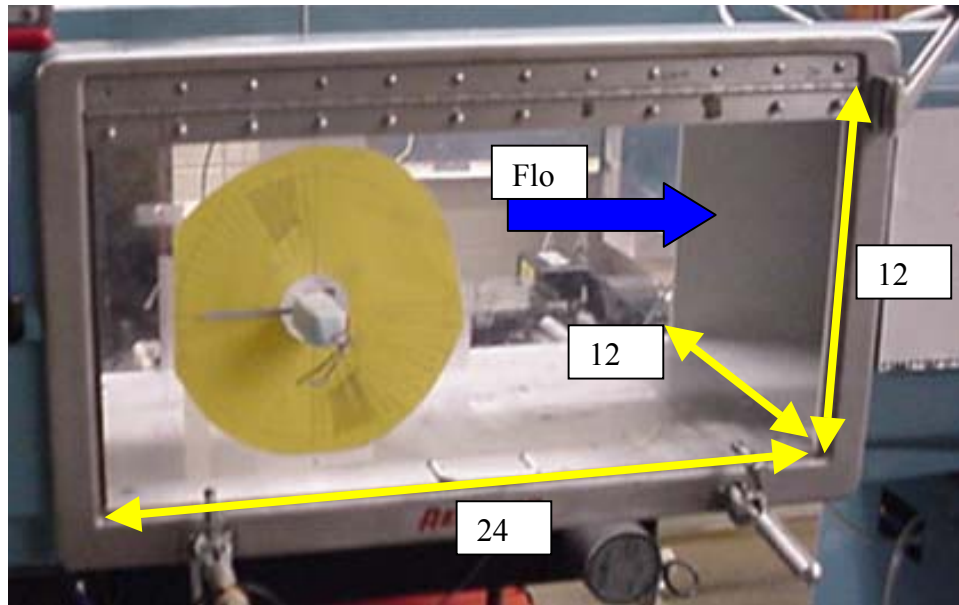


Figure 18. Test Section Dimensions

Four static pressure ports (one on each wall) are located at the entrance of the test section. A pressure transducer measures the dynamic pressure by calculating the difference between the static pressure at the inlet to the stagnation or total (atmospheric) pressure of the flow. Flow velocity is calculated directly from this dynamic pressure and is displayed on a digital readout in mi/hr on the tunnel's control panel. Desired flow velocity is obtained by varying fan speed. It should be noted for future researchers looking to use this facility that the tunnel's integrated pressure transducer used to display flow velocity has considerable drift over time. To this end, the display is good only to get into the ballpark of a desired velocity. A secondary system must be in place to accurately measure flow velocity in the test section.

Instrumentation

A variety of instrumentation was used to perform the tests necessary for this research, as well as much more to gather the required data. First, two types of pitot tubes were used, a relatively large wake pitot and a much smaller boundary layer pitot. Both these instruments were connected to a validyne pressure transducer to measure dynamic pressure for calculation of the flow velocity at a given point. These instruments are seen in the figure 19.

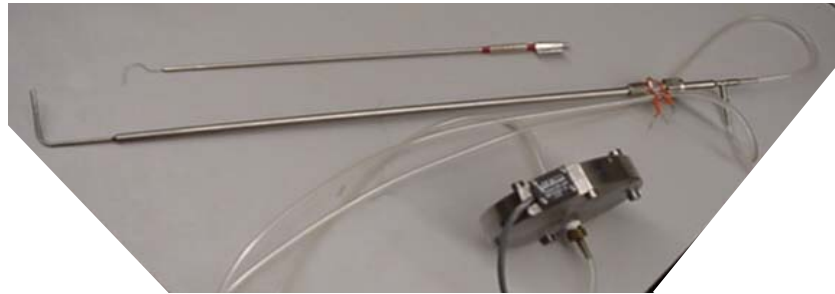


Figure 19. Wake and Boundary Layer Pitot Tubes With Pressure Transducer

The larger wake pitot has both stagnation and static pressure ports. This allows direct measurement of the dynamic pressure with only one instrument. The boundary layer pitot on the other hand is only able to provide stagnation pressure. Because the MEMS were attached, placing static taps on the surface of the cylinder (which would have been ideal) would have been very difficult. By placing the wake pitot at a fixed point in the tunnel, its static pressure capability was used. This caused some problems in the data collection, which will be discussed in a later chapter. The pressure transducer is a device that measures the pressure difference between two inputs through the deflection of a diaphragm in a positive or negative direction (hence the positive and negative sides

of the transducer). The stagnation pressure is attached to the positive side and the static pressure is normally attached to the negative side. The particular transducer used converts the amount of deflection in the diaphragm into a zero to eight-volt signal. Because the changes in boundary layer characteristics when the MEMS were applied were expected to be small, the transducer has a high sensitivity. To this end, it has a pressure capability of 0 to 0.035 inches of water ("H₂O) (0 to 0.889 mmH₂O). This works out to be a maximum of 12 m/s flow velocity capability (a secondary reason for the flow velocity chosen). The transducer has a 200% over-pressure capability but was rarely if ever taken above the 100% level. The calibration of this device will be discussed later.

The next means of data collection was in the form of a hot wire. For this experiment a boundary layer hot wire was used. A schematic of which can be seen in figure 20.

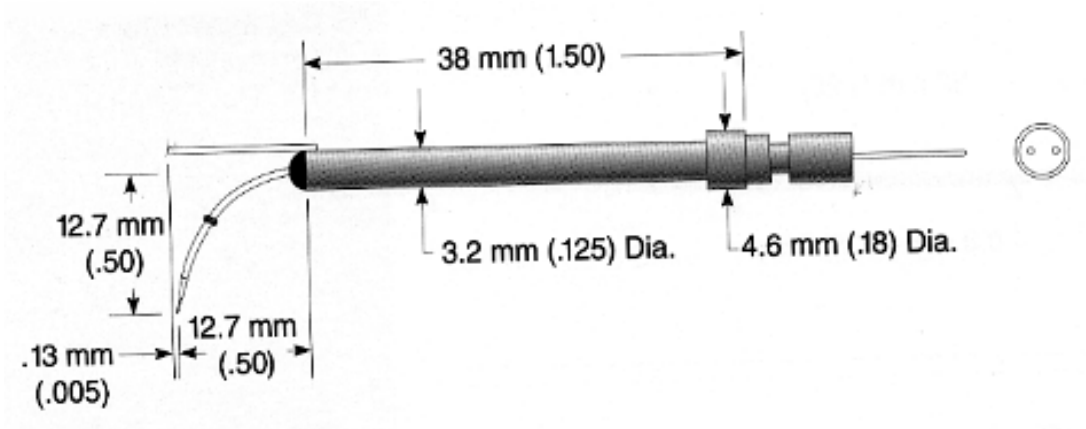


Figure 20. Standard Boundary Layer Hot Wire. (TSI Incorporated).

The hot wire works by trying to keep a very small wire suspended between two contacts at a constant temperature. The higher the velocity of flow over the wire, the faster it will cool and therefore require more current to maintain its temperature. The

current required to maintain a certain temperature can then be directly related to the velocity of the flow through a form of King's law. (White, 1991). The IFA – 100 shown in figure 21 is the control device for the hot wires.

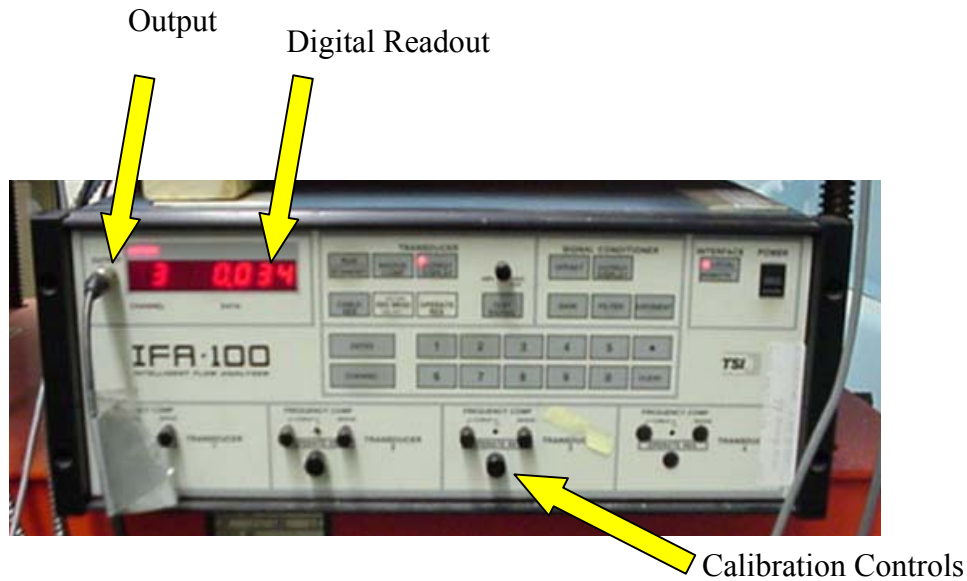


Figure 21. IFA – 100 Hot Wire Control Device

The IFA – 100 feeds the data to the computer system for acquisition via the output cable. The digital readout gives a visual display of the voltage drop across the hot wire sensor.

Data Acquisition Systems

To capture required data, the software program LabView was used. LabView is a data acquisition package, created by National Instruments, Inc., which allows the user to write programs called a virtual instrument (VI). It is a graphical programming language that consists of a front panel and a block diagram. The front panel is the space used by the user to set controls and read outputs. The front panel of a VI is very similar to the

front panel of a real instrument. Every front panel will have an associated block diagram which serves as the source code. (Johnson, 1994). To input information to the system for use by a VI, data must be routed through a data acquisition card. This is a card that is inserted into the computer and attaches to a communication port. Voltage signals were inputted to the system through a National Instruments AT-MIO-16E 12-bit data acquisition card. (National Instruments Inc, 1996).

IV. Methodology

Angular Location and Coordinate System

To understand the rotation and position of both the MEMS and the data collection devices used in this study, a coordinate system needed to be devised that could be used for all practical tests. Although only one will be presented here and all data presented in this thesis will conform to this one, there were in fact three different coordinate and naming conventions used throughout this study. The system used changed as the nature of the testing took on new parameters that the current coordinate system could not take into account or became cumbersome to use. The final coordinate convention is one that will work for any test conceived from here on.

The relative size of the MEMS to that of the cylinder was somewhat arbitrary since no previous work had been performed. It was desirable to keep the arc-angle (ϕ) less than 10 degrees. With the MEMS positioned on the surface of a 25.4mm circular cylinder, ϕ is approximately 5.6 degrees.

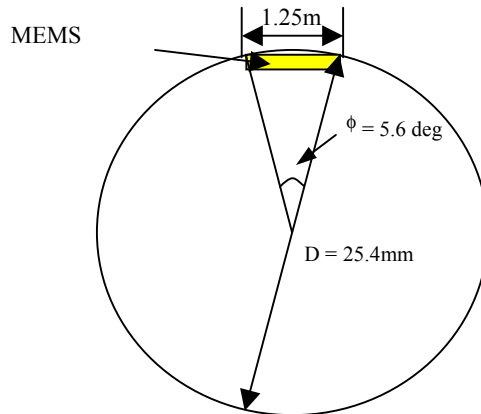


Figure 22. Arc-Angle of MEMS on Circular Cylinder (not to scale)

The angular location deals with the location of the MEMS on the surface of the cylinder. It is measured in degrees and is denoted as the Greek symbol γ . Measuring $\gamma = 0^\circ$ at the stagnation point on the front of the cylinder and proceeding around the top surface of the cylinder gives the angle the MEMS form with the flow. For example, directly into the flow is $\gamma = 0^\circ$, directly on top is $\gamma = 90^\circ$, and directly behind the cylinder is $\gamma = 180^\circ$. This corresponds to θ shown in figure 5. The x,y,z coordinates are defined in the following manner. The x – axis is used to determine streamwise location. It is parallel to the flow in the test section, and positive x is in the downstream direction of the flow (toward the fan). The y – axis determines spanwise location. It is perpendicular to the flow and parallel along the length of the cylinder. Finally, the z – axis defines the displacement above (or below) the cylinder. The origin (0,0,0) is located at the $\gamma = 90^\circ$ tangent line, 10 cm from the right-hand side of the tunnel wall on the surface of the cylinder.

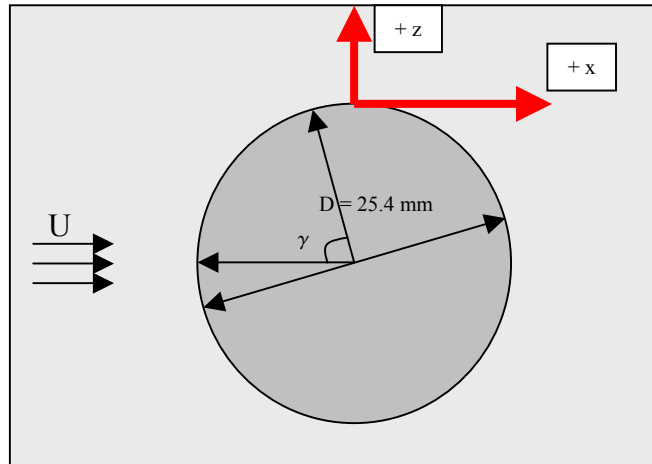


Figure 23. Angular Location and Coordinate Cross Section

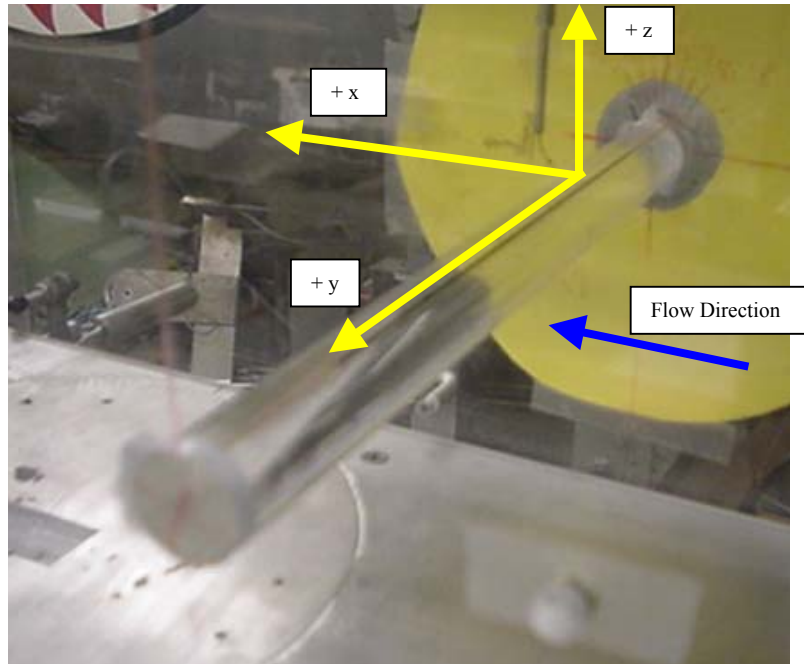


Figure 24. (x,y,z) Coordinate System

MEMS Release, Mounting, Wire Bonding

A large part of the research setup was devoted to the processing of the MEMS devices. Working with MEMS by hand was extremely difficult. Because their size is on the order of μm they are easily broken. To this end, some of the lessons learned for processing will be imparted.

As mentioned before, the MEMS devices come packaged in a protective state. That is, they are coated with a protective photo-resistive layer and the free structures (such as the tabs) are still attached to sacrificial layers. In this condition, they are quite sturdy and can withstand the shipping process. However, in order to use the MEMS as intended, each one must undergo what is known as the release process.

The release process is a chemical process that strips the protective photo-resistive layer, cleans the exposed MEMS devices, and dissolves the sacrificial layers in acid

releasing the MEMS devices, cleaning the devices, and then drying them in a released state. The process was carried out in the AFIT clean room in building 644. This is because of the sensitivity of the devices and the chemicals used in the process. The chemicals used for the process were acetone (ACE) cleaner, methanol (METH), and hydrofluoric acid (HF). The HF is the most critical and dangerous of the three. Because of the health hazard in working with HF, two-person control in the lab had to be maintained whenever HF was in use. An account of the release process steps is given below. This process was set in an assembly line to increase production rate.

Step 1: ACE #1 wash. Place the MEMS in the first ACE container for 15 minutes.

Periodic, vigorous agitation of the MEMS is encouraged to ensure a complete stripping of the photo-resistive layer.

Step 2: ACE #2 wash. Move the MEMS into the next wash of ACE for 10 minutes. This ensures clean solution to fully remove the photo-resistive layer. Care must be taken not to touch the top of the MEMS structures because, although not yet released, they are exposed and can be damaged easily. Periodic mild agitation can be used.

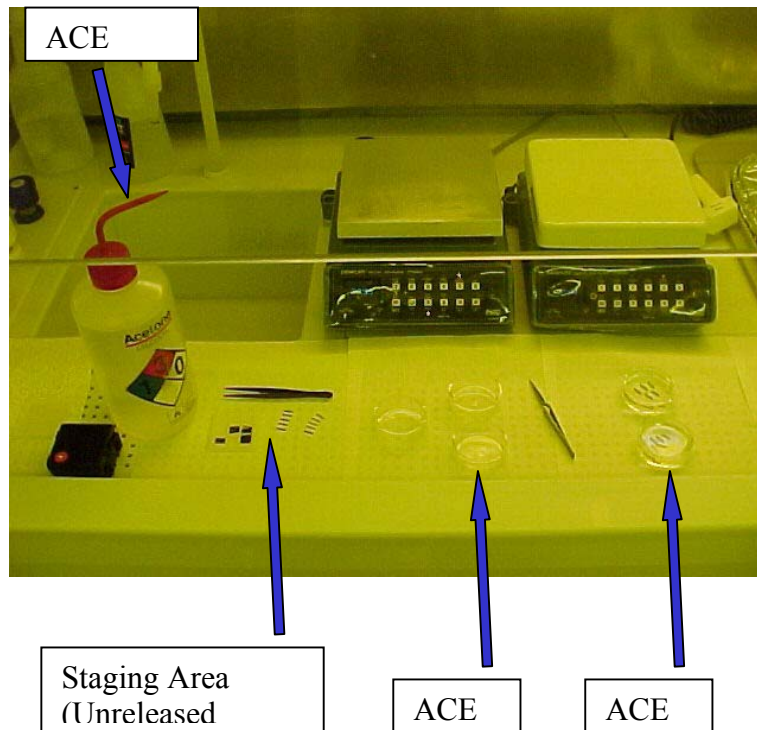


Figure 25. Acetone (ACE) Phase (MEMS Release Process)

Step 3: METH #1 wash. After ACE #2 the MEMS were placed in a METH bath for 10 minutes. This wash cleans excess ACE from the devices. Again periodic mild agitation will help the cleaning process.

Step 4: HF bath. Once the METH #1 wash was complete, the MEMS were ready for the acid wash. It is suggested that each MEMS device be exposed to the HF bath individually. Each device should be exposed to HF for 2 to 2.5 minutes. This is the most time critical step in the process. Once the sacrificial layers are removed and the devices become released, the acid etching process does not stop. The HF will continue to "eat" the structures as long as it is in contact. Due to the hazardous nature of HF, extra precautions were taken to ensure safety when dealing with the chemical. These included

wearing a heavy-duty rubber apron, heavy-duty rubber gloves and a face shield. The time in the wash was measured using a stopwatch and the devices were held using Teflon coated tweezers (HF dissolves metals).



Figure 26. Timed HF Bath (MEMS Release Process)

The release of the MEMS can be visually detected by looking for a color change in the devices, indicating a change in angle of the MEMS to the light source in the room. This is due to the natural curl the devices possess. Very light to no agitation is required for this step. Note: HF should only be placed in a plastic container since it will dissolve glass.

Step 5: METH #1. Immediately after the HF bath, the MEMS should be placed in the METH 1 bath for 5 minutes. This will remove the excess HF from the devices and stop the etch process. Very light agitation can be used to help the cleaning; however, care must be taken now that the MEMS devices are released and free. Forces acting in the wrong direction due to fluid motion over the MEMS can be enough to damage or even strip them from the surface. The solution in the METH #1 container should be replaced approximately every 5 MEMS structures released. This will minimize the amount of HF

concentration in the solution and ensure the etching process is stopped when new devices are placed in the solution.

Step 6: METH #2. The MEMS can now be placed in the final solution in the process.

They will soak in METH #2 for 30 minutes or longer. This ensures a thorough cleaning of all other chemicals and particles remaining on the structures. Again, now that the devices are released, only periodic light agitation is recommended.

Step 7: The last step in the process of release is the drying of the MEMS devices. This is an important but tricky proposition when dealing with MEMS because of their scale. If the METH is evaporated too quickly, the chemical on the surface of the devices will boil and could potentially cause enough stress on the devices to damage or destroy them. If the METH is allowed to evaporate too slowly, due to surface tension, the MEMS devices will remain attached to the "bubble" of METH that is between it and the substrate. As the bubble grows smaller the MEMS structure will be pulled down until it touches the substrate. This phenomenon is known as striction and accounts for many of the failed yields encountered in MEMS production. Drying was accomplished by placing the MEMS one at a time on a hot plate set at 55° C for approximately 15 seconds. Striction still is a concern, but could sometimes be remedied by re-soaking the device in METH 2 for a few minutes and then re-drying. Care must be taken to hold the device securely when placing the MEMS on the hot plate. The METH on the bottom of the structure that initially comes in contact with the plate could evaporate so quickly that a rapidly rising pocket of METH gas creates a force strong enough to flip the structure over destroying the devices on top. Figure 27 shows a microscope view of the released MEMS with one that has been destroyed in the release process.

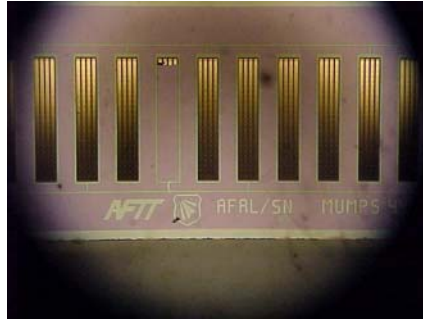


Figure 27. Released MEMS Devices

The bright area indicates the side that is anchored with the deflected end shown as the dark region.

Mounting was accomplished by milling a groove onto the 25.4 mm diameter cylinder. This groove was slightly deeper and wider than the depth and width of the substrate structure. This allowed the MEMS to be counter sunk so that theoretically only the MEMS devices were above the surface of the cylinder in the boundary layer. The following figure shows the theoretical case cross section view of the cylinder with the MEMS in place.

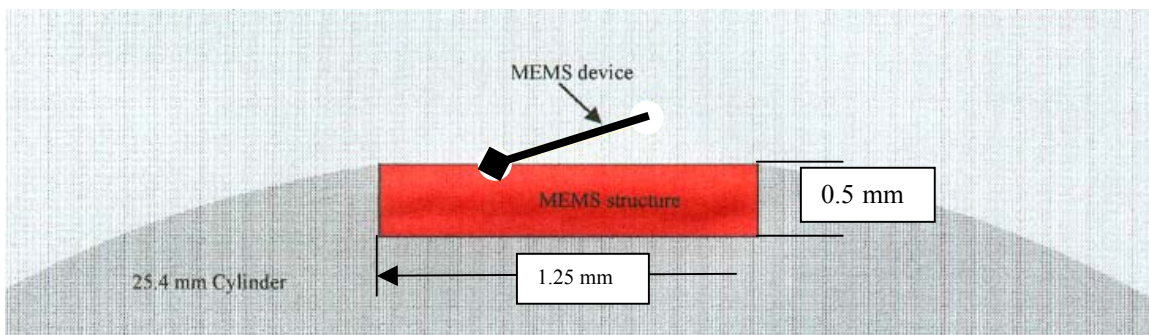


Figure 28. Theoretical Cross Section of Mounted MEMS Devices

Due to the fact that the MEMS were placed by hand the theoretical case is unrealistic. The ideal way to place the MEMS onto the cylinder would be prior to

release, when they are structurally sound and relatively safe to handle. At this time direct pressure can be applied to the top surface without damage. Because of the drying restrictions discussed above, no practical solution to release after mounting was found. The MEMS were placed into the groove onto a bead of glue via tweezers while under a microscope. The sides of the MEMS structure were then pressed down using two razor blades, one on either side of the devices, to level the structures evenly and flush with the surface of the cylinder. Due to error in visual acuity from looking through a microscope and unsteadiness of the human hand, perturbations exist in the levels at which the top surfaces of the MEMS structures truly are. Although not measured precisely, the perturbations were estimated to vary from 0 to 150 μm with the 0 plane being at the surface of the cylinder. This perturbation difference exists not only from one MEMS structure to the next, but across a single structure as well. The overall effect of this "bump" in the cylinder can be seen in later chapters when the passive state is compared to the clean cylinder case.

To apply power to the MEMS, they must be electrically connected to a power source. As shown earlier in chapter 2, there are electrical contacts on both sides of a MEMS structure. Because of this, MEMS can be powered from either side, or daisy chained together to create a long line. Daisy chained devices act as a circuit in parallel, and therefore requires the same amount of voltage for one or for twenty. For this experiment, 20 structures were wired end to end in the following fashion.

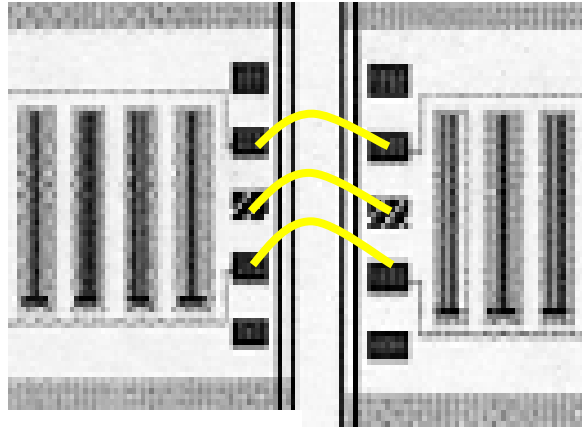


Figure 29. Electrical Connections Between Adjacent MEMS Structures

Wire bonding is done with a wire-bonding machine and uses approximately 10 μm diameter gold thread to make the connection from one contact pad to the next. Larry Callahan of AFRL/SN provided wire-bonding services. For future support in this area, he can be contacted at (937) 255-51874 ext. 3056.

With the release process finished, and the MEMS mounted on the cylinder, testing of the devices could begin.

Testing

The first order of business in the testing of the MEMS devices was to characterize their performance. As stated before, the HF portion of the release process is time critical. Too much time in the acid solution can begin to degrade the devices on top of the MEMS structure. If the conductors on the MEMS are degraded, then the resistance will increase and render the devices useless. Using the MEMS probe station in the AFIT device characterization lab, the values in Table 1 were obtained.

Measured Parameter	Value
Resistance from positive to positive - R	13.6 k Ω
Resistance from ground to ground - R _g	10 Ω
Pull down voltage for long MEMS	80 V
Hold down voltage for long MEMS	60 V

Table 1. MEMS Electrical Properties

The pull down and hold down voltage of the MEMS describe how much voltage it takes to activate them, and how much it must be relaxed to disengage them. For example, to actuate the MEMS from their passive (up) state, to their active (down) state, 80 volts of power must be applied (pull down voltage). The MEMS will stay in this state until the voltage is relaxed to less than 60 volts (Hold down voltage). In order to actuate the MEMS at a desired frequency, the voltage provided must oscillate between 80 volts and less than 60 volts. The Hewlett Packard function generator used for this purpose supplies a 4 Volt Peak-to-Peak (VPP) sine wave that is sent through a x20 amplifier to amplify the input signal to 80 VPP. Once the MEMS devices characterization was complete, the cylinder and MEMS were mounted into the tunnel, suspended in the test section from the sidewalls of the tunnel.

Because of the fragility of the MEMS, damage during the mounting and wire bonding process was a problem. This left the configuration shown in figure 30 of MEMS spanwise across the cylinder for testing.

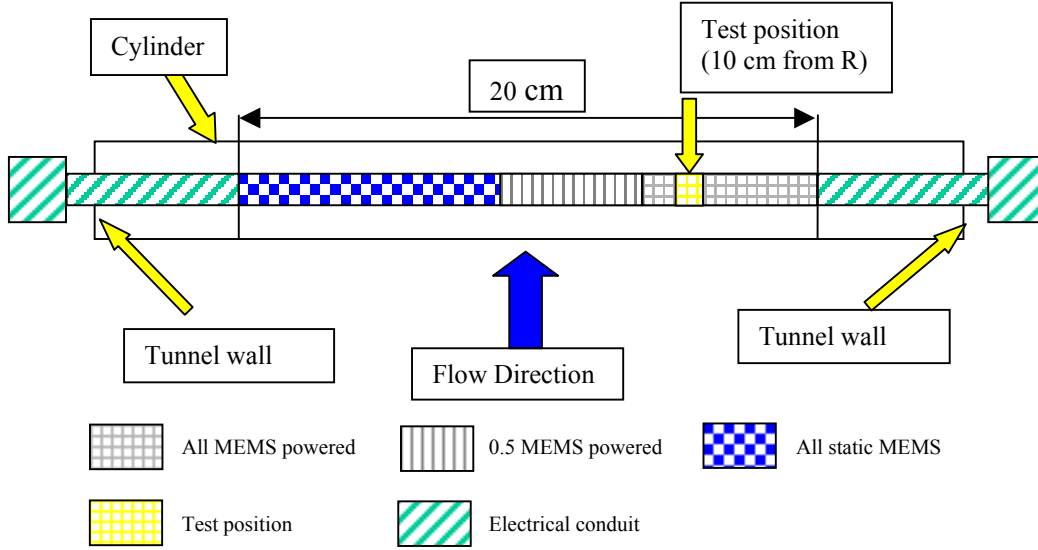


Figure 30. Map of Spanwise MEMS Layout on Cylinder

From the right, due to a break in the electrical connection that could not be fixed, only six structures had the capacity for all 47 MEMS devices being actuated. The test position (as marked) was selected for this reason and this location was also the furthest to the right the traverse system could extend without hitting the side of the tunnel ceiling. With the y - axis defined as extending parallel along the length of the cylinder, this position was defined as $y = 0$. The next five centimeters are filled up with structures that can only actuate every other device. The rest of the structures, due to a total breakdown of electrical connectivity, are passive only. Due to the above conditions, data collection was almost exclusively accomplished at $y = 0$.

With the data collection device (either pitot tube or hot wire) at the $y = 0$ location the following three basic conditions were investigated in this study: the clean cylinder, MEMS passive at some angle γ (as defined earlier) into the flow, and MEMS active at some frequency (f) and some angle γ into the flow. With these three cases being the

general conditions, of course, a variety of γ 's and f 's were investigated to find the optimal value for each. Three streamwise locations were investigated for boundary layer effects: $x = 0$ (which corresponds to the 90° mark on the surface of the cylinder), $x = 6.35$ mm (which corresponds to the 120° mark on the surface of the cylinder), and $x = 18$ mm (which corresponds to 5.3 mm behind the cylinder in the wake), as shown in figure 31.

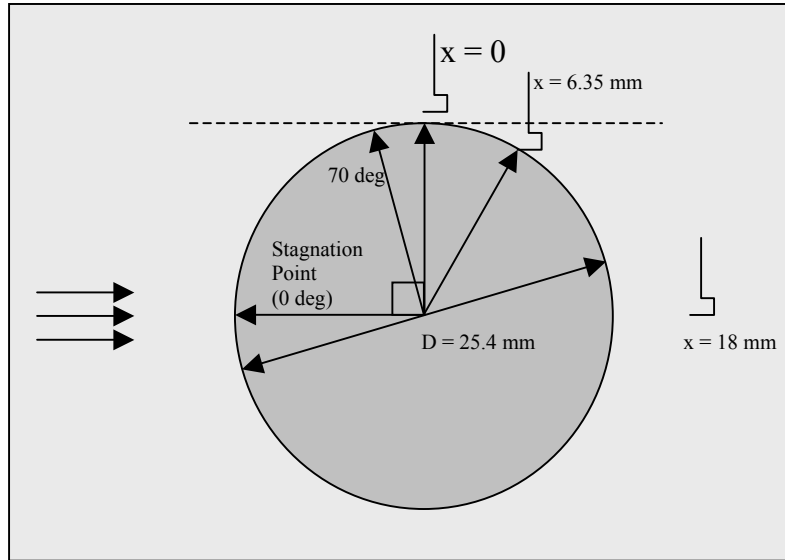


Figure 31. Measure of Data Acquisition Points

The line tangent to the $\gamma = 90^\circ$ position on the top of the cylinder, in figure 28, represents the $z = 0$ (up/down axis) line. The three "hook" symbols represent the data acquisition device being used.

The angle γ was measured using a large circle with degrees marked off on the side. This was centered on the rotation axis of the cylinder and a pointer was attached to the end of the cylinder as shown in figure 32.



Figure 32. Angle Measuring

From the boundary layer pitot, data acquisition was gathered at a rate of 1000 samples/second with 15,000 samples/channel. This data was gathered after a 15-second wait period between each data point to allow for equalization in the pitot lines to occur. Consequently, each data point with the pitot tube represents 30 seconds of data. The hot wire data rate was set at 50,000 samples/channel with a data rate of 10,000 samples/second. Consequently, each data point with the hot wire represents 5 seconds of data.

Both probes were mounted on a three-axis traverse system with the location measured with a Sony LH61 measurement system good to $\pm 0.5 \mu\text{m}$.

V. Data Reduction

LabView produced raw data files that were reduced into various plots and values. Output data for the velocity and fluctuation data files included two sections, the heading information and data sets. The heading included such information as the file name (i.e. 08 Feb 02, Profile Test 01), and column headings. The heading also included the atmospheric pressure, given in inches of Mercury (inHg), at the time of the test and the sample rate at which data was taken. The data section included the data taken at each point sampled. It is displayed in columns, and includes information about the position, the local measured velocity, turbulence levels, and temperature.

08 Feb 02, Profile Test 01			
P atm (inHg)	29.135		
sample rate	10000	#samples/ch	50000
Position (mm)	HW U (m/s)	Tu %	flow temp (F)
-1.6365	0.3238	53.6854	68.6999

Table 2. Sample Format of Data

Table 2 is a representation of the data presented when the raw data file is opened in an excel spreadsheet. As mentioned earlier, the position data is an absolute position measured from a zero plane using a Sony measuring system accurate to 0.5 microns. Excel was used extensively in manipulating data into the various plots that are seen in this chapter. MatLab was used to plot Fast Fourier Transform (FFT) data saved for specified data points during testing. The FFT data presents a picture of the frequency response of the flow. This was the primary means of experimentally measuring the shedding frequency of the cylinder. Although Excel was used to manipulate data for comparison reasons, MatLab was also used to plot the velocity and turbulence data for

each individual data set. The MatLab code for the above calculations can be seen in Appendix A: Data Acquisition/Manipulation.

Air Density (ρ)

The air density used in all calculations was calculated using the ideal gas law. (Cengel, 1998).

$$\rho = \frac{P}{R \cdot T} \quad (6)$$

where

P = Atmospheric pressure (Pa)

R = Gas Constant (0.2870 kJ/(kg*K))

T = Air temperature (K)

The atmospheric pressure is measured using a digital barometer shown in figure 33.



Figure 33. Digital Barometer

The readout from the barometer was in inches of Mercury (inHg). This was converted into the appropriate units using the conversion:

$$1 \text{ inHg} = 3.387 \text{ kPa} = 3387 \text{ Pa} \quad (7)$$

The temperature was given by a digital thermocouple readout shown in figure 34.



Figure 34. Digital Temperature Readout

The display is given in degrees Fahrenheit, which needed to be converted into the Kelvin scale. This was accomplished by first converting into degrees Celsius by the following conversion:

$$^{\circ}\text{C} = (^{\circ}\text{F} - 32)/1.8 \quad (8)$$

Degrees Celsius was then converted into the appropriate Kelvin value by the following conversion factor:

$$\text{K} = ^{\circ}\text{C} + 273.15 \quad (9)$$

Leaving ρ from equation 6 in desired units of kg/m^3 . (Cengel, 1998).

Bernoulli's Equation

When using the pressure transducer connected to a pitot tube (wake or boundary layer), the flow velocity was calculated directly from Bernoulli's Law shown in equation (10). The wake pitot uses the stagnation and static pressures measured at the tip of the pitot. The boundary layer pitot uses the stagnation pressure measured at the tip of the pitot, whereas the static is that measured approximately 50 mm above the surface of the

cylinder. As stated before, the problems that arise from this will be discussed in a later chapter.

$$P_{\text{stagnation}} - P_{\text{static}} = \frac{1}{2} \rho U^2 \quad (10)$$

The differential pressure transducer gives the pressure difference ($P_{\text{stagnation}} - P_{\text{static}}$). Using ρ from the ideal gas law, the velocity (U) can be solved for by rearranging Bernoulli's equation into the following form:

$$U = \sqrt{\frac{2 (P_{\text{stagnation}} - P_{\text{static}})}{\rho}} \quad (11)$$

King's Law

Kings Law can be used to predict heat transfer from the surface of a cylinder in cross flow and is shown in equation 12.

$$q_w = a + b \cdot \sqrt{U} \quad (12)$$

where

a and b = constants found by calibration in known flow conditions

U = free steam velocity

As stated before, a hot wire uses a form of King's law to solve for flow velocity. For a wire acting as a cylinder in crossflow, a current (I) passed through that wire placed normal to the flow direction with velocity (U), then the current will be a measure of U.

Alternately, if the current is held constant, then U can be predicted and King's law takes on the following form:

$$I^2 = a + b \cdot \sqrt{U} \quad (13)$$

In King's law a and b are constants that are found by calibration in a known flow velocity. (White, 1991).

VI. Results and Discussion

Boundary Layer Pitot Tube Data

Because the optimal position of the probe at this stage of the tests was unclear, a boundary layer (BL) pitot was used to allow greater flexibility in movement without the danger of breaking a hot wire. Testing with the BL pitot was conducted in the following manner. By stepping the MEMS through a variety of angles from 90° to 45° as well as using three significantly different frequencies of actuation and comparing each to a clean cylinder case, it was possible to see a spread in the plots for the different cases as shown in figure 35. Only the 90° to 60° plots are shown below because the $\gamma = 45^\circ$ plot is much the same as $\gamma = 60^\circ$.

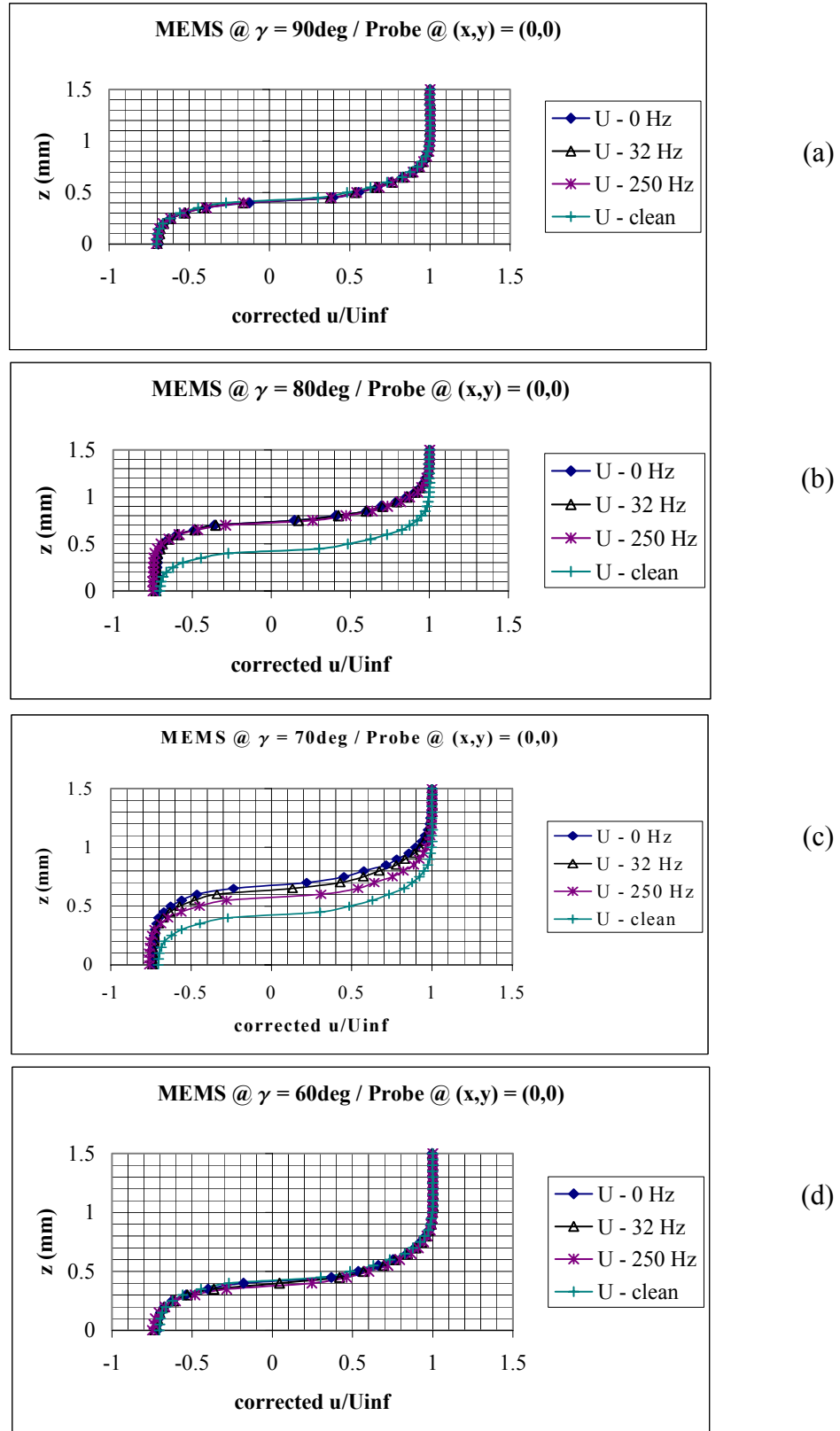


Figure 35. Boundary Layer Pitot Tube Data (a) $\gamma = 90^\circ$ (b) $\gamma = 80^\circ$ (c) $\gamma = 70^\circ$ (d) $\gamma = 60^\circ$

Figure 35 shows boundary layer traverses using a boundary layer pitot tube from the surface of the cylinder ($z = 0\text{mm}$) to $z = 1.5\text{ mm}$. For each plot set, the MEMS were actuated at a variety of frequencies for a set angular location.

In figure 31 (c) the spread in graphs at $\gamma = 70^\circ$ were of great interest. This was an indication that there was an effect in the flow being created by the MEMS, prompting more exploration. The above data was obtained using a boundary layer pitot tube. Because of the physical setup of the test section, it was difficult to tap the surface of the cylinder to obtain a static pressure reading in the boundary layer. This caused a problem for the reading of data. Because of the size of the wake pitot, it was placed approximately 50 mm above the surface of the cylinder as noted earlier in this paper. With a fixed static pressure reading as a reference plane, in the boundary layer there is a case when the stagnation pressure is less than the free stream static pressure. From Bernoulli's equation, this results in a negative flow velocity (U), which physically is impossible. Manually manipulating the data acquisition programs allowed the acquiring of this data and to plot the physically unrealistic negative velocity. Although quantitative statements about this data cannot be made, they are useful in the suggestion of trends to investigate.

With a clear trend in the data discovered, the means of data acquisition was then converted to a hot wire to provide more detailed information about the flow in the region of interest. Using the pitot data from the $\gamma = 70^\circ$, a static hot wire position was selected at 0.5 mm above the surface of the cylinder because of the greatest difference in the plots representing the different frequencies as related to each other and the clean cylinder case.

Hot Wire Data at 8 m/s

Using static hot wire data with the free stream of the tunnel set to 8 m/s, the task became finding the optimal angle for which the MEMS could provide the greatest amount of adjustment in the flow.

Previous data showed minimal effect caused by the MEMS above the 90° and below the 60° position. The data therefore starts at 90° and steps through to 60° , for a variety of frequencies of actuation. This of course is referenced to the clean cylinder case (with the MEMS rotated to $\gamma = 180^\circ$). The γ angle showing the greatest shift in the plot data of the different frequencies was $\gamma = 69^\circ$. This is seen in figure 36.

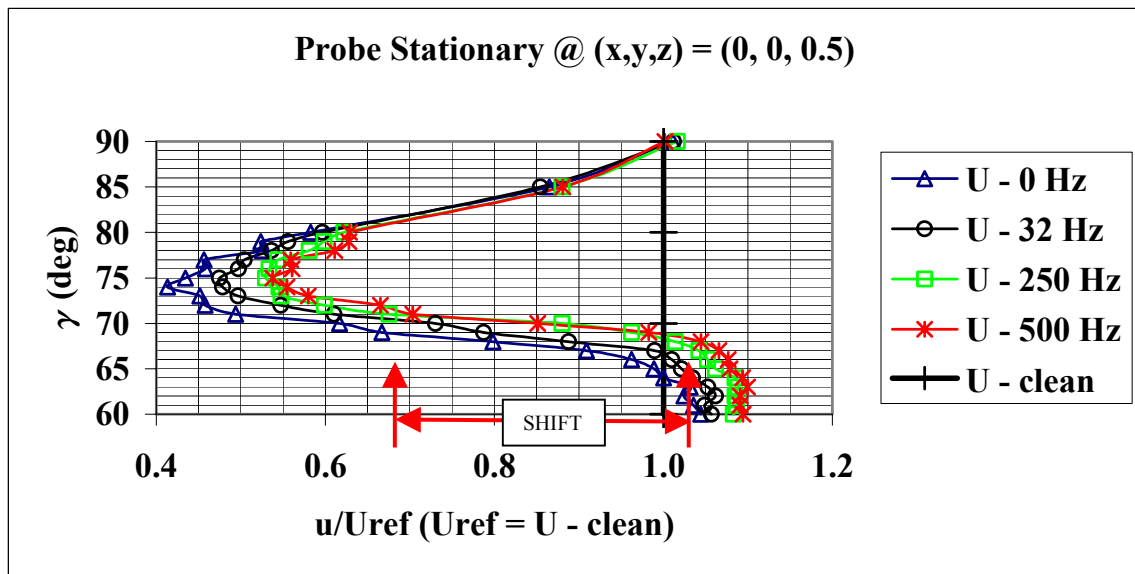


Figure 36. Static Hot Wire (Determining γ Optimal)

Figure 36 shows curves of various frequencies of operation with changes in angular location (γ). The probe is stationary at 0.5 mm above the surface of the cylinder. The curves are a representation of non-dimensionalized velocity Referenced to the clean cylinder case, the gamma (γ) optimal value that provided the greatest shift in the plots

was found to be 69 degrees. The same procedure as above was used to find the optimal frequency at $\gamma = 69^\circ$. This data can be seen in figure 37.

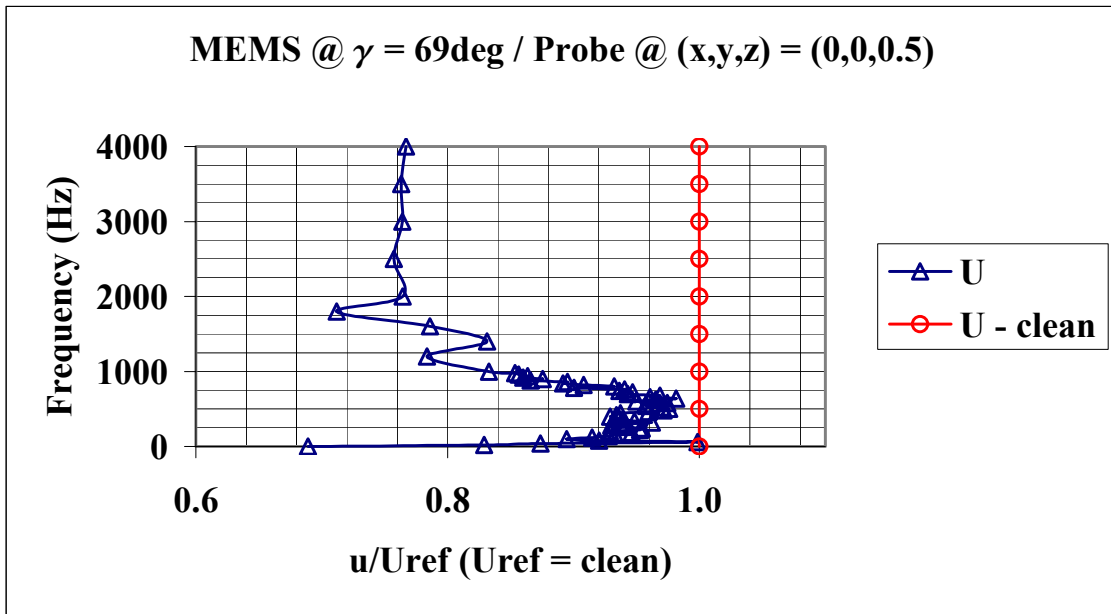
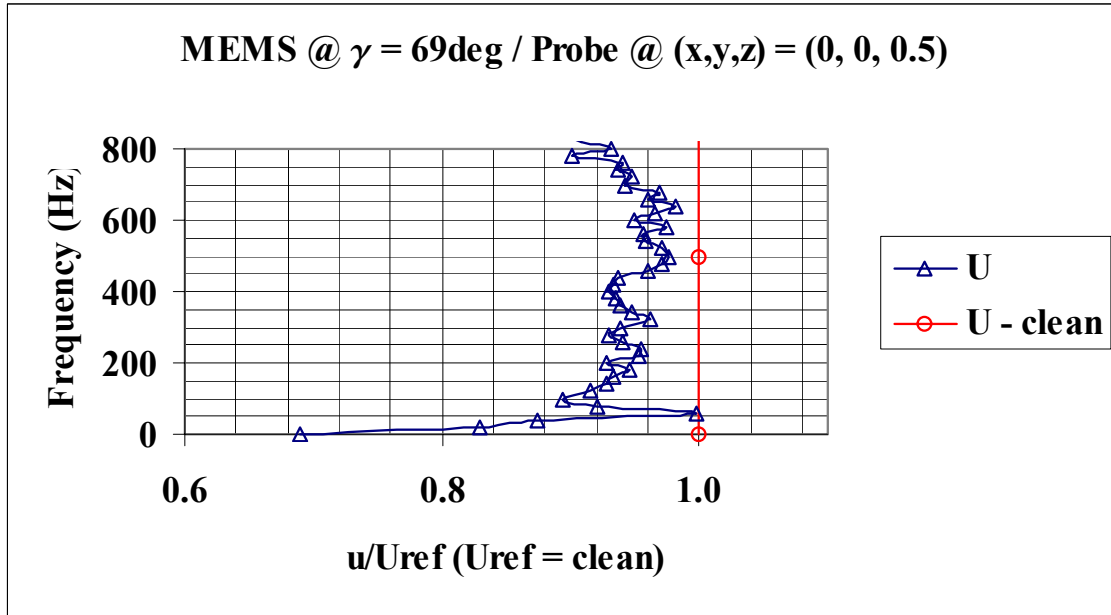
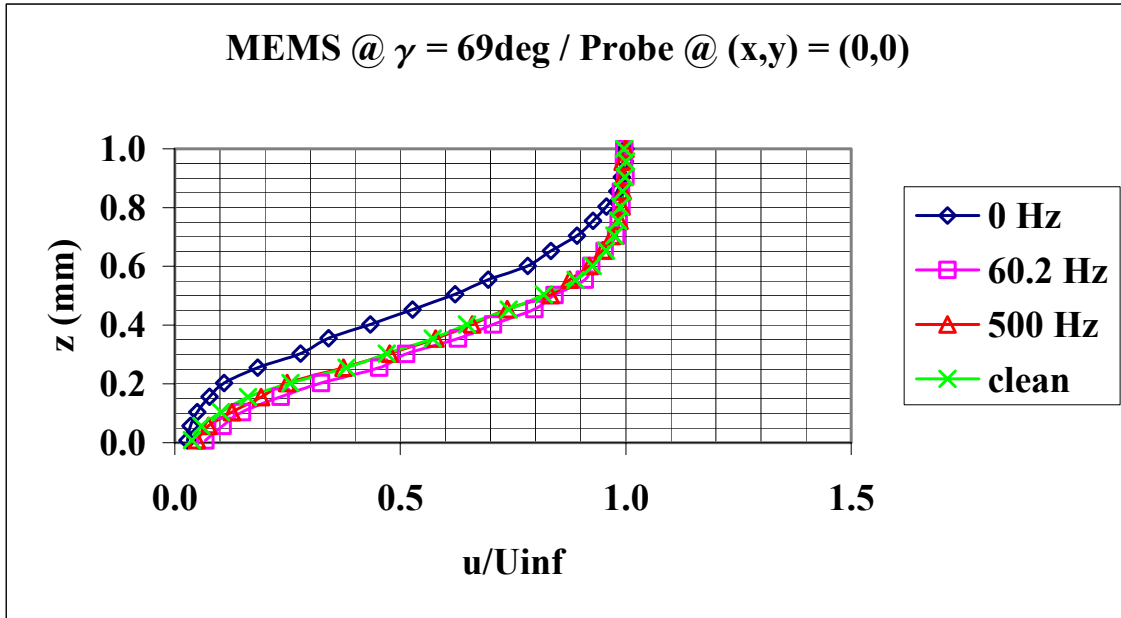


Figure 37. Static Hot Wire (f_{Optimal}) (a) Full frequency range (b) 0 to 800 Hz

It can be seen in figure 37 that there is a strong inflection point at around 500 Hz, and there is also a spike point at 60 Hz. This frequency is near the shedding frequency of the cylinder at the flow velocity of 8 m/s. This shedding frequency was found using the theoretical Strouhal number as well as found experimentally which will be shown later in this chapter.

Detailed wake and boundary layer data was taken at this setting to characterize the level to which forcing at this frequency could induce changes to the boundary layer. The data in figure 38 shows boundary layer plots with the hot wire traversing at $x = 0$, $x = 6.35$ mm, and in the wake at $x = 18$ mm (5.3 mm behind the cylinder).



(a)

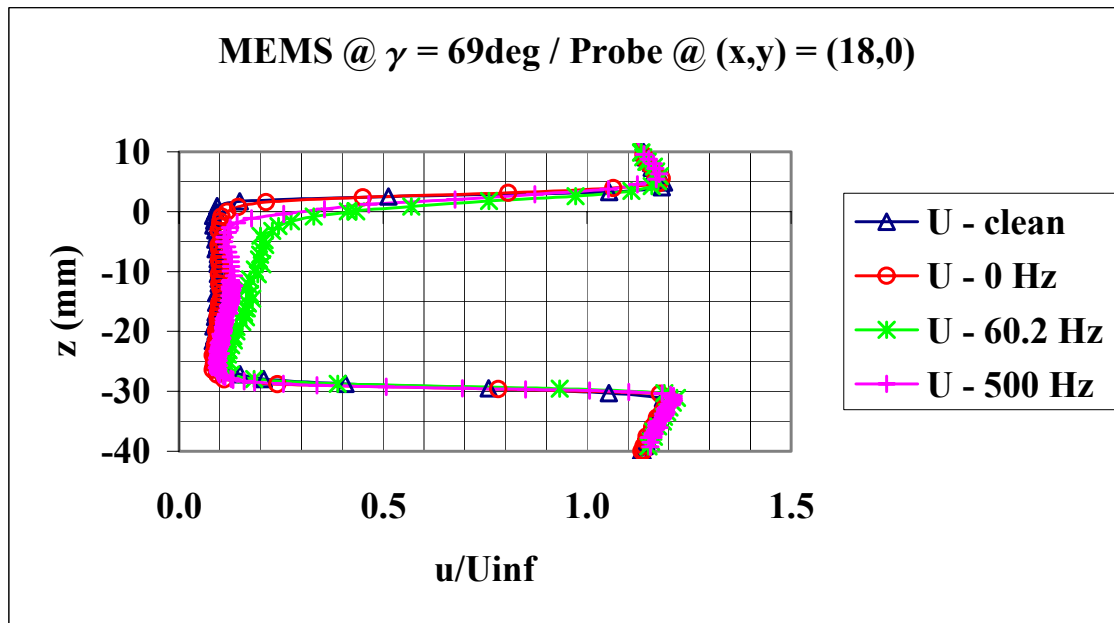
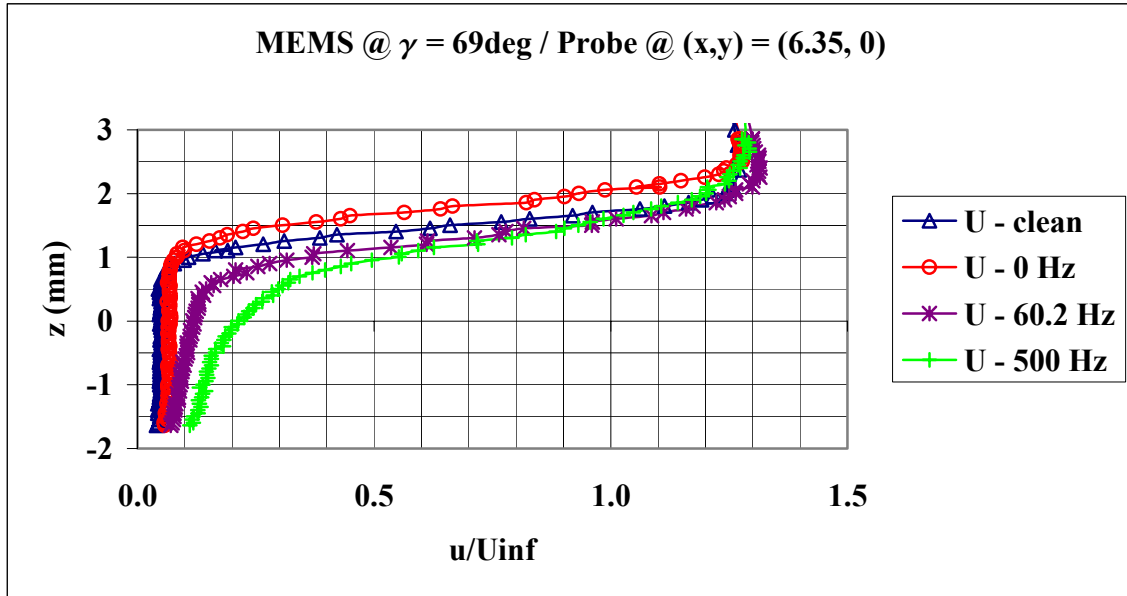


Figure 38. Hot Wire Probe (Wake Profiles) a) $x = 0$ mm b) $x = 6.35$ mm c) $x = 18$ mm

It can be seen in figure 34 that the momentum deficit is reduced from the clean cylinder case to that of the MEMS placed at $\gamma = 69^\circ$ and actuated at 60.2 Hz. The above

graphs were integrated using wake theory to find θ_{wake} . The integral equation used is a slightly different form of the boundary layer momentum thickness equation. Here θ_{wake} is known as the momentum thickness of the wake and is set up as the following:

$$\theta_{\text{wake}} = \int_0^{\infty} \frac{\Delta u}{U_{\text{inf}}} \left(1 - \frac{\Delta u}{U_{\text{inf}}} \right) dz \quad (14)$$

where:

$$\Delta u = (u - U_{\text{inf}}).$$

U_{inf} = Free Stream Velocity

For the purpose of this experiment, the integration was done from $z = -12.7$ mm to + infinity rather than from – to + infinity. (White, 1991). This was done because the wake forms due to MEMS effects are asymmetric and the top is the region of interest. The results of the integration can be seen in table 3.

x (mm)	Clean	0 Hz	60.2 Hz	500 Hz
0	-0.5441	-0.7542	-0.4849	-0.5359
6.35	-5.7423	-6.1461	-5.0479	-4.4780
18	-26.3007	-25.8831	-19.8078	-23.0260

Table 3. Integrated Wake Values (θ_{wake})

The Integral method used to obtain the values in table 3 is for turbulent wakes. Because it is certain that the boundary layer remains laminar throughout these tests, the separation point occurs at approximately 80 degrees. (White, 1991) For this reason, probes used to acquire data are in a turbulent wake and the boundary layer momentum thickness equation did not bring out the desired effect that was seen in the velocity plots. It is apparent that as the wake extends downstream, the forcing frequency able to

maintain an effect on the flow is the shedding frequency. Figure 39 gives an idea of where the above data would be located in relation to the cylinder.

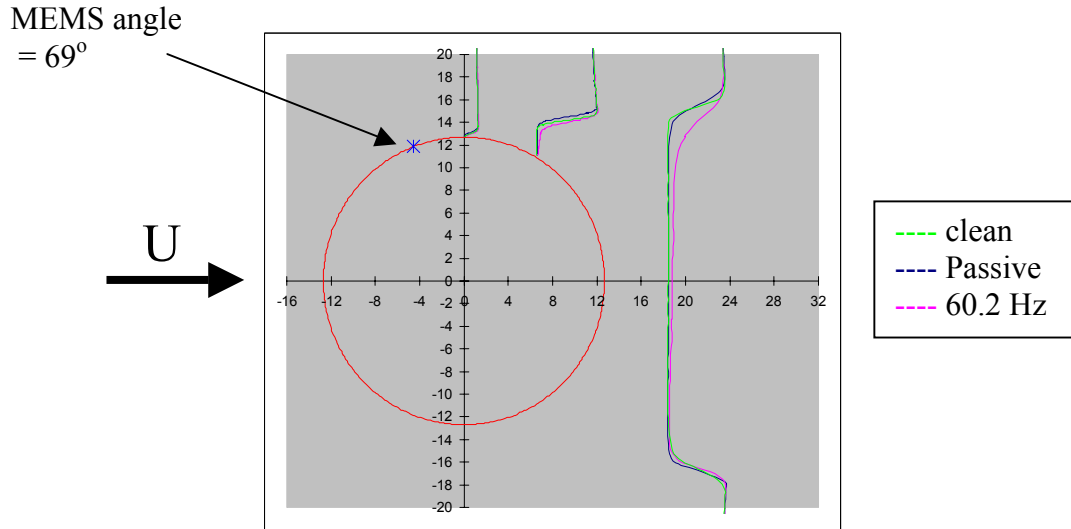


Figure 39. Position of Data Relative to Position of MEMS Devices

The boundary layer can be visualized growing into a wake pattern that spreads out larger as it propagates downstream.

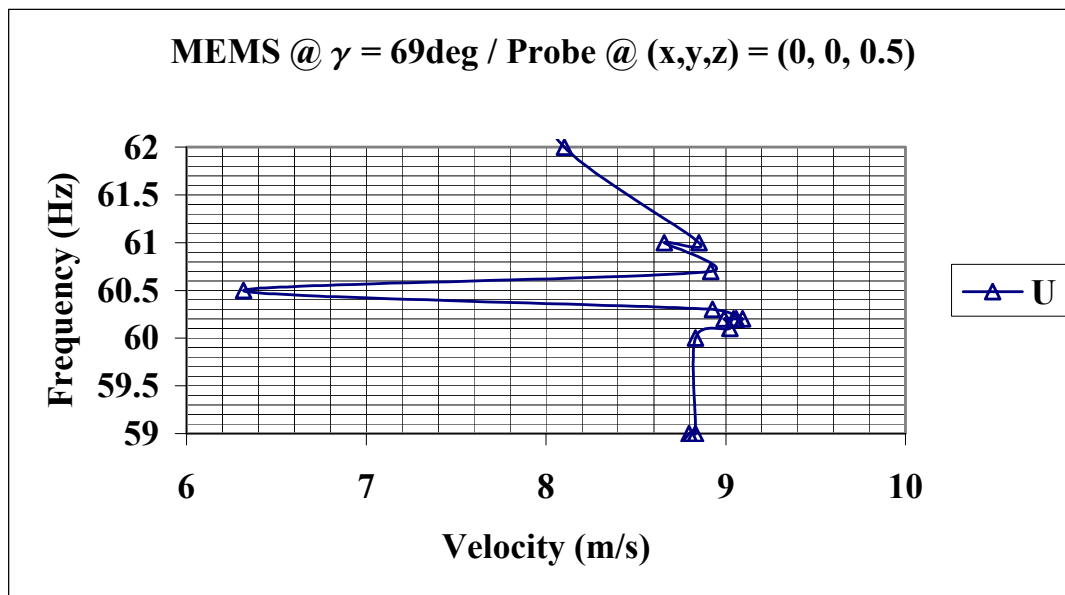


Figure 40. Frequency Sensitivity Analysis

This optimal frequency was found to be very sensitive to slight variations on the order of 0.2 Hz (as seen in figure 40). The greatest effect was found to appear at an operational frequency of 60.2 Hz. This is approximately that of the shedding frequency of the cylinder found experimentally to be $f = 60.4$ Hz. Using FFT data and averaging the measured peaks from 6 different tests found this frequency. This is seen in figure 41.

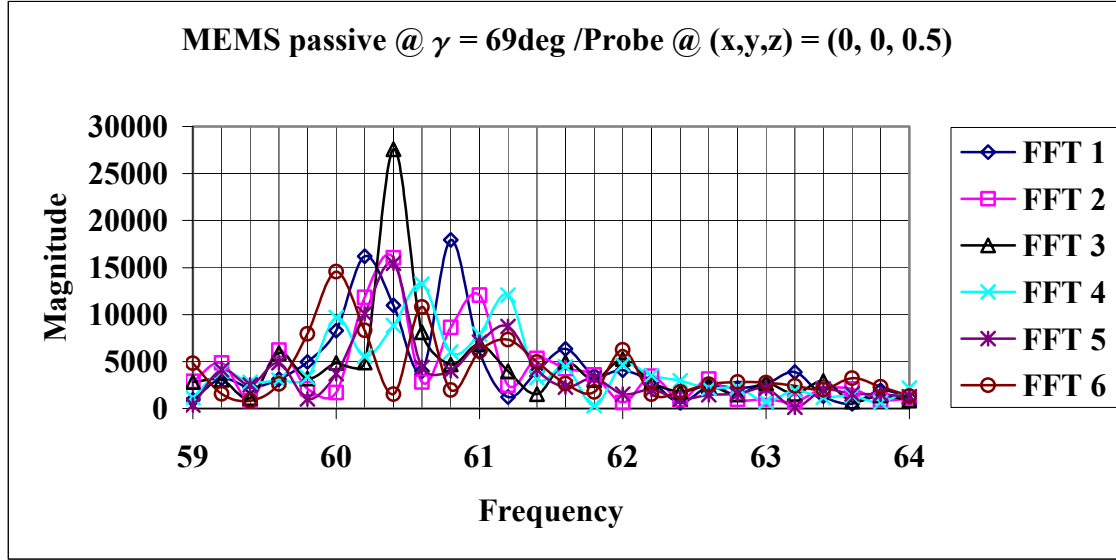


Figure 41. Experimental Shedding Frequency

Theoretically, using the Strouhal number for 8 m/s, the shedding frequency should be $f = 63\text{Hz}$. Because the $St = 0.2$ value is an approximate value, the non-matched experimental values for shedding frequency to the theoretical prediction was not surprising. The effect of frequency response shown in figure 42 for the following three cases: Clean, 0 Hz (passive), and active at $f_{\text{opt}} = 60.2$ Hz.

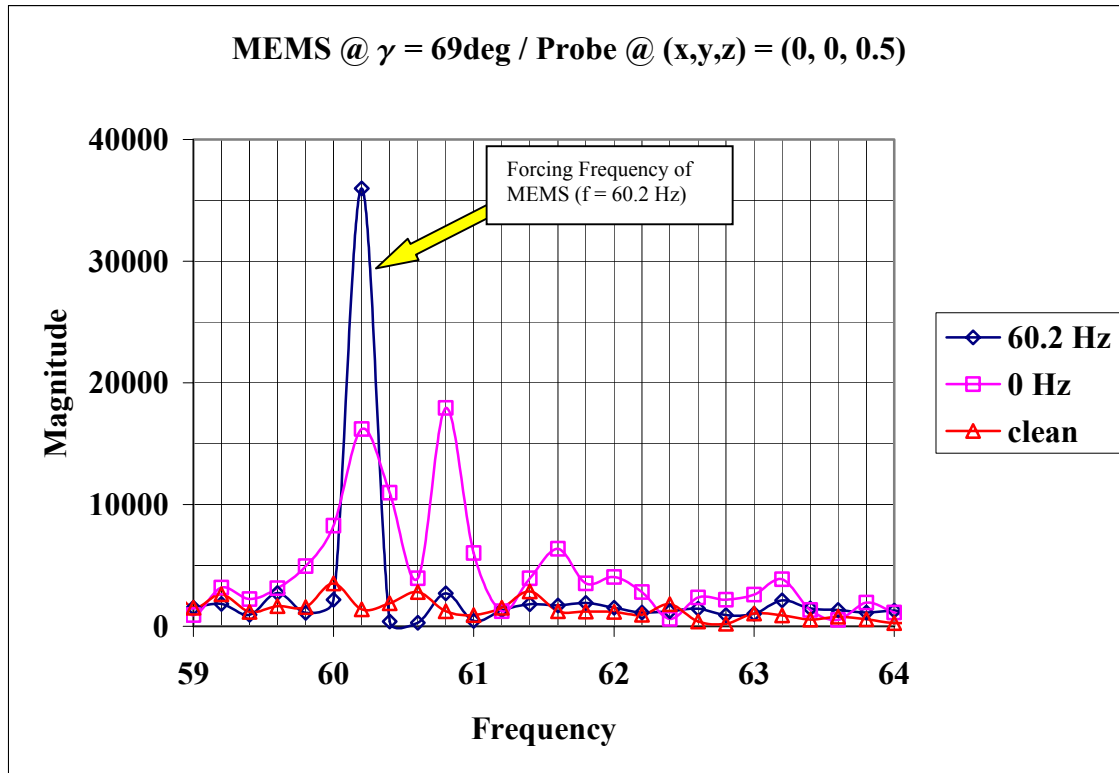


Figure 42. FFT Frequency Signal from Hot Wire Data

With the sensitivity of the operating frequency determined, a series of tests were performed to provide information about the sensitivity to changes in angle γ .

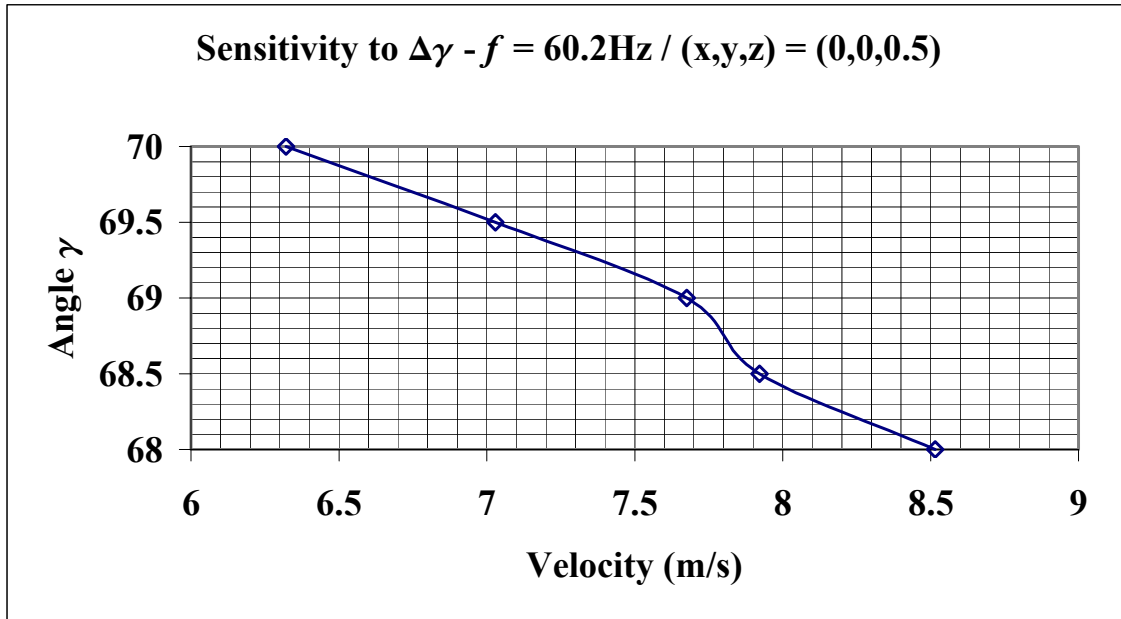


Figure 43. Sensitivity Analysis to Changes in γ

It can be seen in figure 43 that very slight changes in the angular location of the MEMS on the cylinder produce significant changes in momentum. Changes on the order of 0.5 degrees can cause a 1 to 1.5 m/s difference in the velocity.

The interesting finding is that the flow over the cylinder is most susceptible to forcing by the MEMS if the actuation is performed at the shedding frequency of the cylinder.

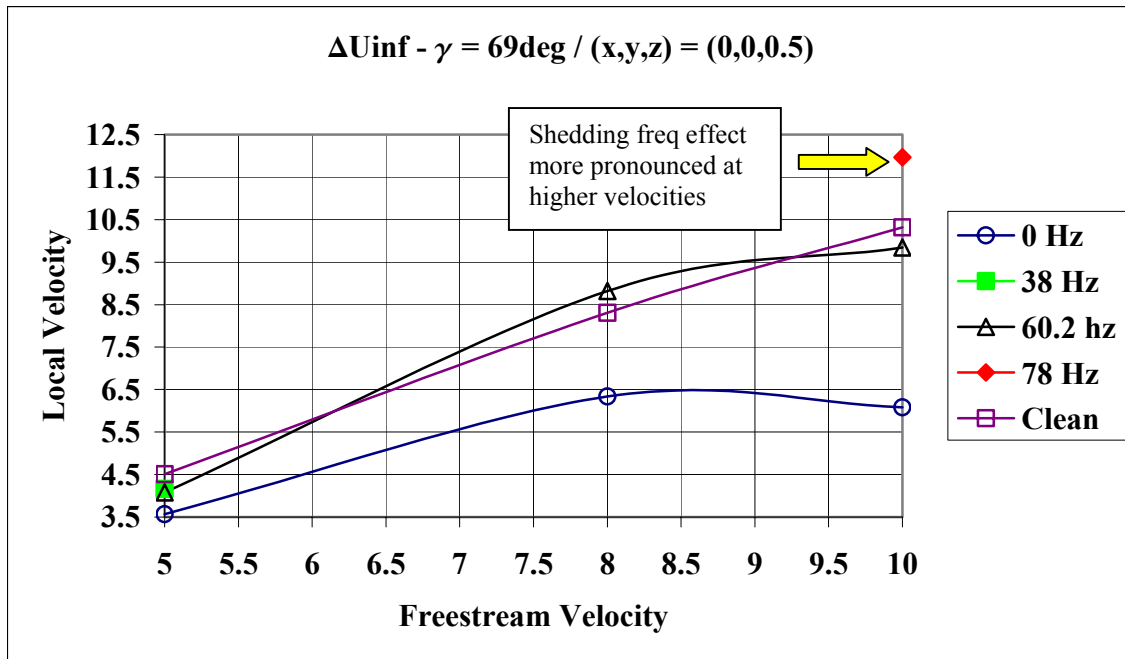


Figure 44. Effects of Changing Free Stream Velocity

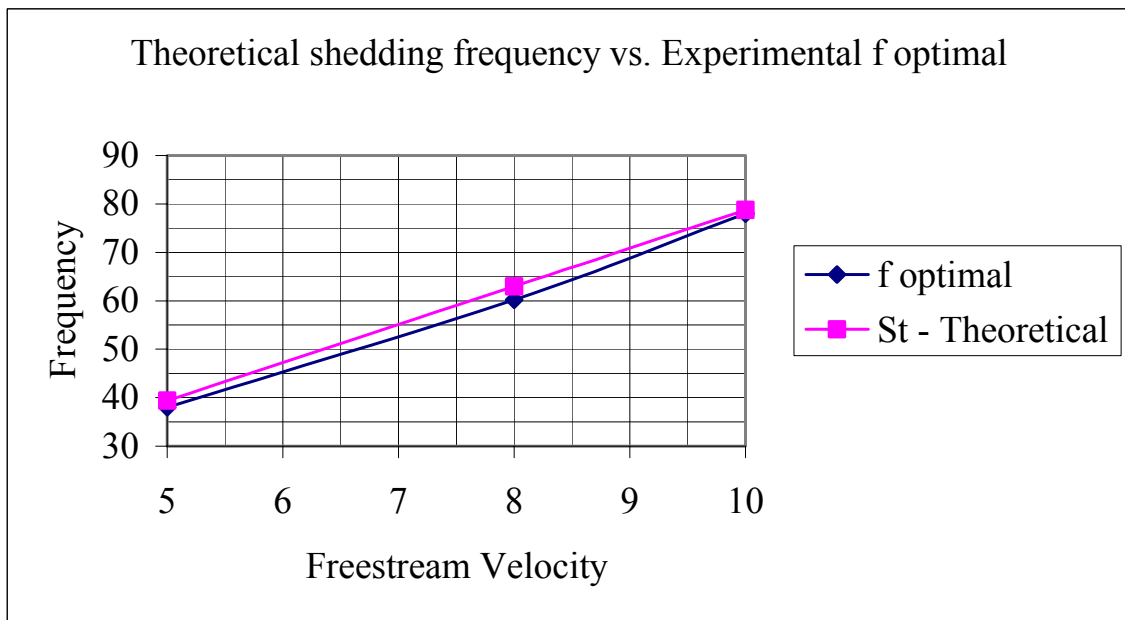


Figure 45. Theoretical Shedding Frequency vs. f Optimal

Figures 44 and 45 show that at flow velocities of 5 m/s and 10 m/s the trend of greater effect at the shedding frequency still exists. They also indicates that the greater

the flow velocity the more pronounced the effect becomes. Similar tests as those just laid out run at higher tunnel velocities suggest the same trends. In figures 46 and 47, the optimal angle γ is still equal to 69° . The forcing frequency also follows the shedding frequency of the cylinder as expected. The experimental shedding frequency was measured at $f = 74$ Hz and the $f_{\text{opt}} = 74.2$ Hz.

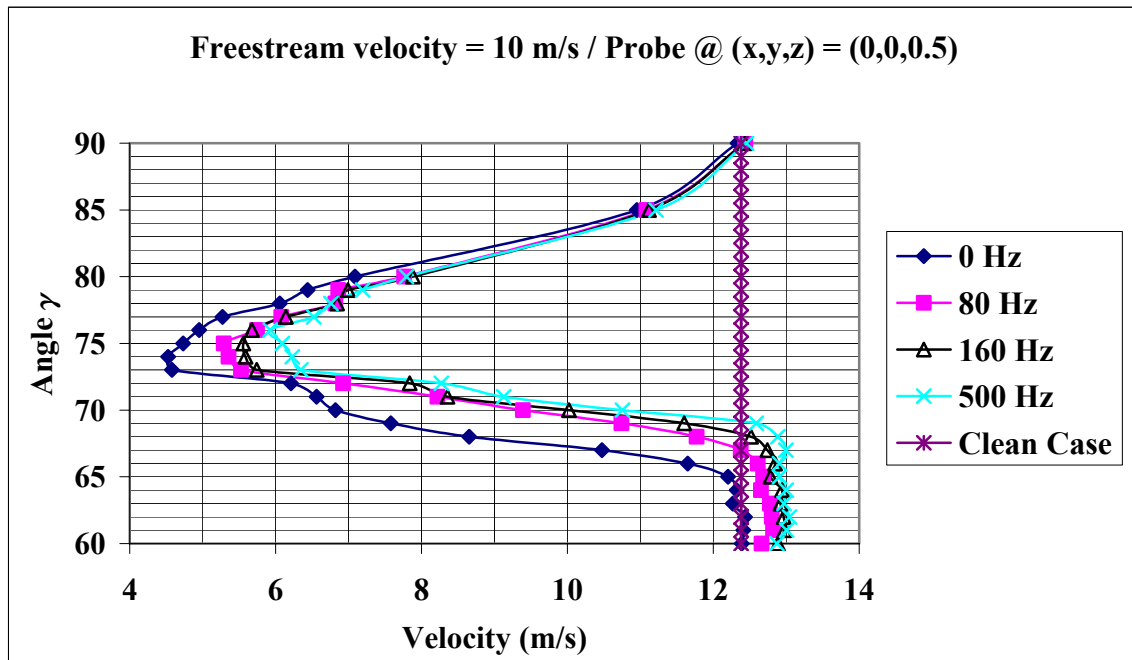


Figure 46. γ_{opt} at 10 m/s

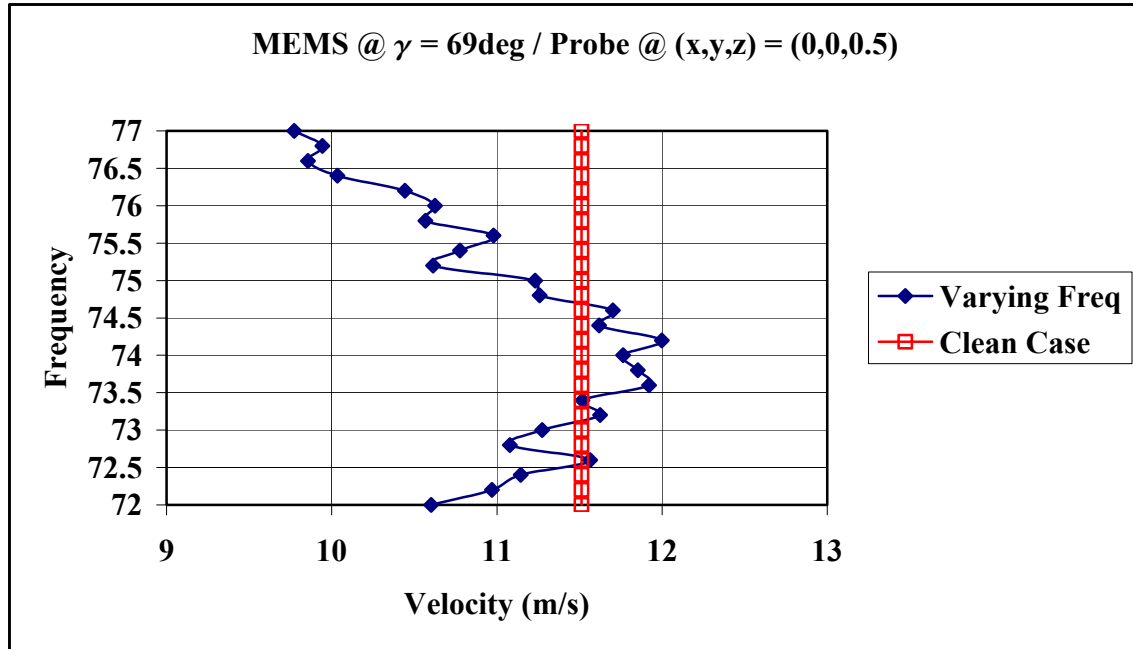


Figure 47. Optimal frequency at $\gamma = 69\text{deg}$

The interesting phenomenon that occurs is that the optimal γ angle remains the same, where as the optimal f changes with velocity. This will be explored in more detail in the next chapter; however, it suggests the angle γ may be dependent on the location of the boundary layer separation point, whereas the operating frequency f is dependent on the vortex shedding frequency.

Error Analysis

In order to say anything conclusive about any of the data obtained during the course of this study, an error range needed to be established. This error range will be used to describe the amount by which a certain set of data, whether it is a plot or quantitative value, could vary from the data presented.

Error was established throughout the course of the study by obtaining data under the same conditions after a significant lapse of time had occurred (at least one day). During this change in time quite often a parameter of the test subject had been changed and then changed back to the original conditions to copy a test previously obtained. This is known as repeatability. The repeatability of a test also serves as a tool to obtain error in the system, and ensure test parameters could be reset to desired conditions as needed. This error is known as precision, or random, errors. Precision errors are a spread in data points, from a single measurement to the average value of several data points under the same conditions. (Wheeler, 1996). Error is determined by taking the ratio of desired data to a reference point. This is shown in the following equation.

$$E = \left(\frac{P}{P_{\text{mean}}} \right) \cdot 100\% \quad (15)$$

Where

P = Data of interest being referenced.

P_{mean} = Average value of two or more similar data sets.

A single percentage value for the error is determined by obtaining an error for each test case referenced to the mean, then taking the mean value of each error value as seen in equation (16). Where n is equal to the number of data sets being compared.

$$E_{ave} = \frac{1}{n} \sum_{n=1}^n E_n \quad (16)$$

Figure 48 shows a sample graph of data points taken under the same conditions used to obtain the final value of error used against all data used to support the theories and assumptions that have been presented and will be supported in the next chapter. Using repeated test runs from several different data collection techniques and obtaining an error percentage from each, it is possible to obtain an error value that approximately applicable to all data taken in the process. Taking an error value from different data collected from hot wire data and averaging them together, a final error value of plus or minus 1.0% was obtained. This value can be applied to all data collected in this research. The above error calculations are known as precision error and are useful in repeatability analysis. Data used to obtain precision error can be seen in Appendix B.

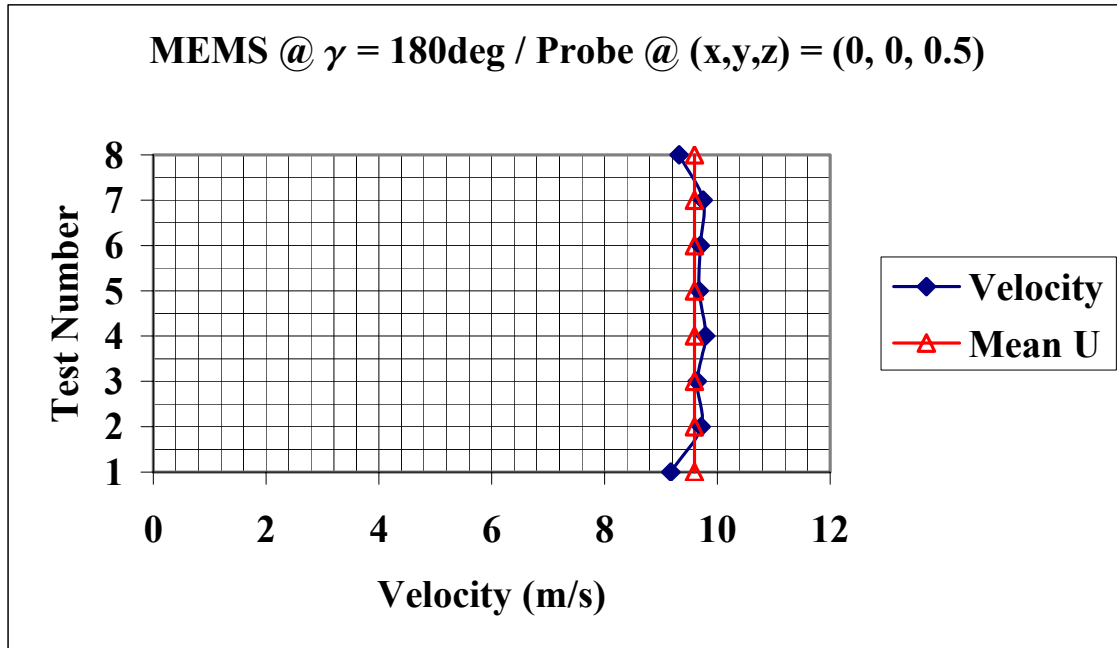


Figure 48. Sample Graph of Data used to Obtain Error

VII. Conclusions and Recommendations

The main focus of this research was to characterize the controlling effects MEMS devices had on flow around a circular cylinder in cross flow. To accomplish this, the optimal angle (γ) had to be determined and the optimal frequency at which to apply forcing had to be found.

The optimal angle was found to be constant. This is due to the location of the separation point. For a laminar flow, the separation point from a circular cylinder is approximately 80° . It makes sense that the optimal angle (γ) is upstream of this phenomenon. An important element is that the optimal forcing frequency of the MEMS devices is that of the shedding frequency. By forcing at the shedding frequency, a 25% decrease in momentum loss of can be gained in the wake of the cylinder. It must be pointed out that the momentum loss of the clean cylinder and that of the passive MEMS at angle γ is not the same. These should be very close to the same but the MEMS are not perfectly flush to the surface of the cylinder, as discussed earlier. The groove that has been placed on the cylinder creates a significant amount of extra drag that must be overcome. Active MEMS can have a significant contribution to decreasing the momentum loss of the flow. If these devices could be positioned as cleanly as possible, it is conceivable that the effect on the flow could be even greater by eliminating the need to overcome much of the extra drag caused by the non-uniformity in the placing of the MEMS on the cylinder.

Recommendations for future studies:

1. Because of time constraints, tests were not conducted with alternating motion of the MEMS devices, meaning when a tab is deflected down, its neighbors

are in the relaxed (up position). This may allow more room for spanwise vortices to be generated by the MEMS devices without much interference with adjacent vortices. The time constraint came down to the need to build an Op Amp that would invert the appropriate signal so the two signals would be exactly 180° out of phase.

2. Testing was done at a angular location of 69° . This was the optimal angle to detect spread in the velocity plots and not necessarily the optimal in which to induce the desired effect on the wake. Because of uncertainty in the data acquisition, the angle that produced the largest spread was selected so as to ensure that any change would be detected. There are lower angles of γ that look very promising in forcing the flow and reducing momentum loss to possibly an even greater extent. It is recommended that testing be done that focuses on the effects at these smaller angles of γ .
3. The tab deflection during actuation could not be measured. Currently there is only a measure of deflection under a vacuum. This may or may not be the actual deflection when actuated. Indeed, the devices may or may not deflect the same amount when actuated at varying frequencies. It is recommended to come up with a scheme to measure deflection at a variety of frequencies of operation. As a suggestion, a high-powered digital video recorder or microscope that could be placed at the viewing window of the wind tunnel.
4. There is no data that gives a clear indication of what the MEMS are actually doing to the flow to reduce momentum loss. Spanwise vortices that are created and propagate downstream are one possibility. It is recommended to

come up with a flow visualization method that would be capable of focusing in on the MEMS level and capture the realities of the flow field that close to the surface. The use of smoke or Schlieren photography may provide a means of visualizing the flow close to the surface.

5. The final recommendation is to use the MEMS that are still in the packaged state. There are 43 notched MEMS that may have a larger effect by creating asymmetry in the vortices produced. It is possible that this may be similar to the effects seen using Vortex Generation Jets (VGJ's) with pitch and skew angles associated with them. These VGJ's have been shown to create a greater effect than jets normal to the surface of the airfoil.

Appendix A: Data Acquisition / Manipulation

Computer: Micron 133 MHz Pentium

Interface Card: GPIB Interface Card (IEEE interface)

Data Acquisition Software: LabView 5.0

Data Acquisition Board: National Instruments AT-MIO-64E

32-Channel Differential Input Board

12-Bit Analog to Digital Conversion

Input Range: -10 to +10 Volts

Gain: 1.0

Precision: 305 μ V

(National Instruments Inc, 1996).

MatLab Code: The following is the program to plot velocity and turbulence data.

% Written by Captain David Borgeson, United States Air Force
% Air Force Institute of Technology (AFIT), November 2001

% This function reads in a specified data file
% and manipulates it into a usable format.
% It finds the 2 maximum data points associated with the velocity data.
% It integrates the area under the velocity curve.
% It then plots the velocity with respect to position.
% The momentum loss is seen as "theta" displayed on the plot.

% Function inputs are:
% XXmonth01testX: Name of data file

% Function outputs are:
% Velocity vs. Position plot with momentum loss value.

% Program loop to continue reading files until told to stop

q = 0;
EOR = 0;

while EOR == 0;

% Define Variables

```
check = 0;
EOH = 0;
R = uigetfile('*. *', 'Pick a file');
fin = fopen(R);
```

% section to avoid header information

```
while EOH == 0;
    nextline = fgetl(fin);
    headline = sscanf(nextline, '%s');
    check = strmatch('Position', headline);
    check > 0;
    if check == 1;
        EOH = 1;
    end
end
```

% section to gather test data

```
i = 1;
while feof(fin) == 0;
    nextline = fgetl(fin);
    data = sscanf(nextline, '%e');
    position(i) = data(1);
    p = transpose(position);
    pt_U(i) = data(2);
    u = transpose(pt_U);
    Tu(i) = data(3);
    turb = transpose(Tu);
    temp(i) = data(4);
    T = transpose(temp);
    i = i + 1;
end
```

```
fclose(fin);
```

% section to perform integration under velocity curve

```
numofsteps = input('Enter number of data points in file: ');
stepsize = input('Enter step size of data points: ');
X = (numofsteps+1)/2;
Y = (numofsteps+1) - 3;
U1 = (sum(u(4:8)))/5;
```

```

U2 = (sum(u((((numofsteps+1)-3)-4):((numofsteps+1)-3))))/5;
U = (U1 + U2)/2;
[max1,index1] = max(u(4:X));
[max2,index2] = max(u((X+1):Y));
F1 = u/U;
F2 = 1-F1;
F = F1.*F2;
n = transpose(index1+3:index2+(X+1));
G = (F(n)+F(n-1))/2;
C = G*stepsize;
theta = sum(C)
thetastring = num2str(theta);

```

% section to plot data

```

top = 13.25;
bottom = 16.75;
M1 = min(u);
M2 = max(u);
z = (M1:0.01:M2);

```

% velocity plot only

```

titlename = R;

figure(q+1);
%hold on;
%plot(abs(p),u,'bx-')
plot(abs(p),u,'bx-', top, z, 'r-', bottom, z, 'r-')
legend('theta = ',thetastring, 4);
%gtext(thetavalue);
title(titlename);
xlabel('position');
ylabel('velocity');
axis([0 28 5 8.5]);
grid on;

```

% both velocity and turbulence plots together

```

turbplot = input('plot Tu with velocity? (Y = 1, N = 0): ');
if turbplot == 1;
    figure(2);
    plot(abs(p),u,'bx-',abs(p),turb,'m*');
    title(R);
    xlabel('position');
    ylabel('velocity and %Tu');

```

```

        axis ([0 28 0 9]);
        grid on;
    end

    q = q + 1;
    progend = input('Plot Another Data Set? (Y = 1, N = 0): ');
    if progend == 0;
        EOR = 1;
    end
end
end

```

The following MatLab code provides a plot of FFT data gathered by the hot wire probe.

```

% Written by Captain David Borgeson, United States Air Force,
% Air Force Institute of Technology (AFIT), February 2002.
%
% This function reads in a specified data file
% and manipulates it into a usable format.
% It plots fast fourier transform (fft) frequency with respect to magnitude.

% Function inputs are:
% DDMMYYt00fft00: Name of data file

% Function outputs are:
% Frequency Vs. Magnitude plot.

% Program loop to continue reading files until told to stop

q = 0;
EOR = 0;

while EOR == 0;

    % Define Variables

    R = uigetfile('*.txt','Pick a file');
    fin = fopen(R);

    % section to gather test data

    NOP = input('Enter number of data points: ');
    size = NOP/2;
    i = 1;
    while i <= size %feof(fin) == 0;
        nextline = fgetl(fin);
        data = sscanf(nextline,'%f');
    end
end
end

```

```

    freq(i) = data(1);
    f = transpose(freq);
    magnitude(i) = data(2);
    m = transpose(magnitude);
    i = i + 1;
end
fclose(fin);

% section to calculate amplitude of the fft signal.

n = NOP;
a = m/(n/2);

% FFT magnitude plot only

titlename = R;
f1x = input('Enter X-scale value for Fig 1: ');
f1y = input('Enter Y-scale value for Fig 1: ');
f2x = input('Enter X-scale value for Fig 2: ');
f2y = input('Enter Y-scale value for Fig 2: ');
figure(q+1);
plot(f,m,'b-')
title(titlename);
xlabel('Frequency');
ylabel('Magnitude');
axis([0 f1x 0 f1y]);
grid on;

% FFT amplitude plot

figure(q+2);
plot(f,a,'m-');
title(R);
xlabel('Frequency');
ylabel('Amplitude');
axis([0 f2x 0 f2y]);
grid on;

q = q + 2;
progend = input('Plot Another Data Set? (Y = 1, N = 0): ');
if progend == 0;
    EOR = 1;
end
end
end

```

Appendix B: Error Determination

The equations used for error determination have been discussed in the body of this thesis. Presented here is the data used to determine the precision error for the different data acquisition techniques.

Wake Pitot

The wake pitot was attached to a validyne pressure transducer with a 0 – 0.035 inH₂O capability. It was a linear transducer with a 0 to 8 Volt output range. The following data sets were used to determine Wake pitot error.

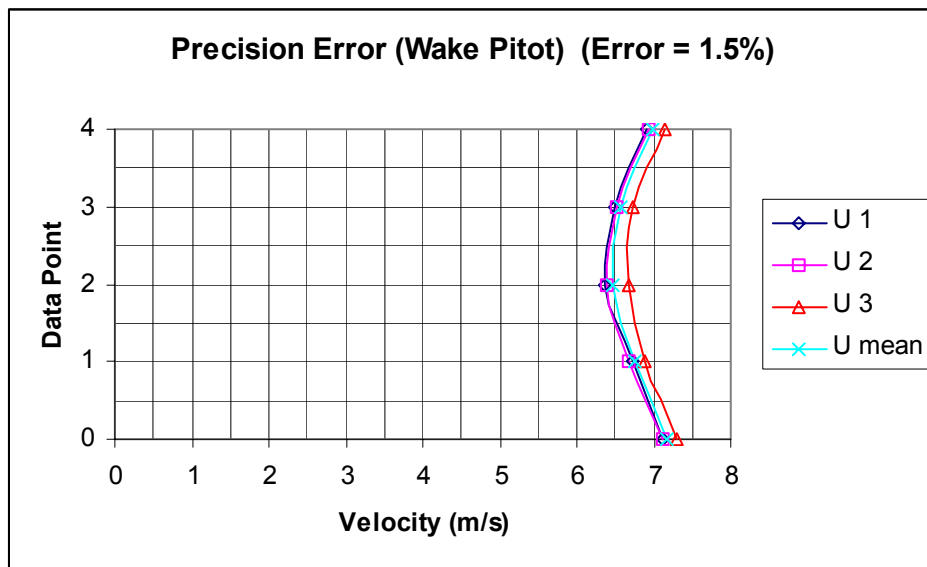


Figure C1. Wake Pitot Precision Error

Boundary Layer Pitot

The boundary layer pitot was attached to the same validyne pressure transducer as the wake pitot. The system required a longer period to equalize the pressure due to the

small opening for the stagnation pressure. For this reason, the error for the BL pitot is not expected to be the same.

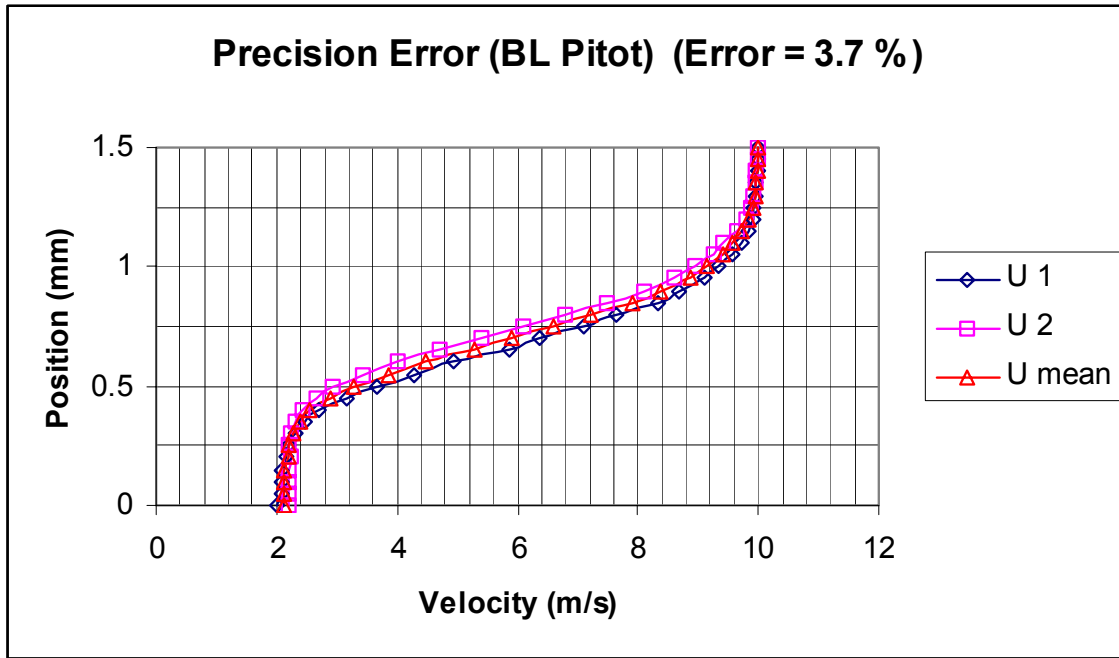


Figure C2. Boundary Layer Pitot Precision Error

The large precision error associated with using the BL pitot comes from the fact that the static pressure is referenced to the free stream which induces error into the system. This measurement is used only in a qualitative sense and not quantitative.

Hot Wire Probe

The hot wire is the most sensitive instrument used. The error associated with this instrument is much less than the other data acquisition probes.

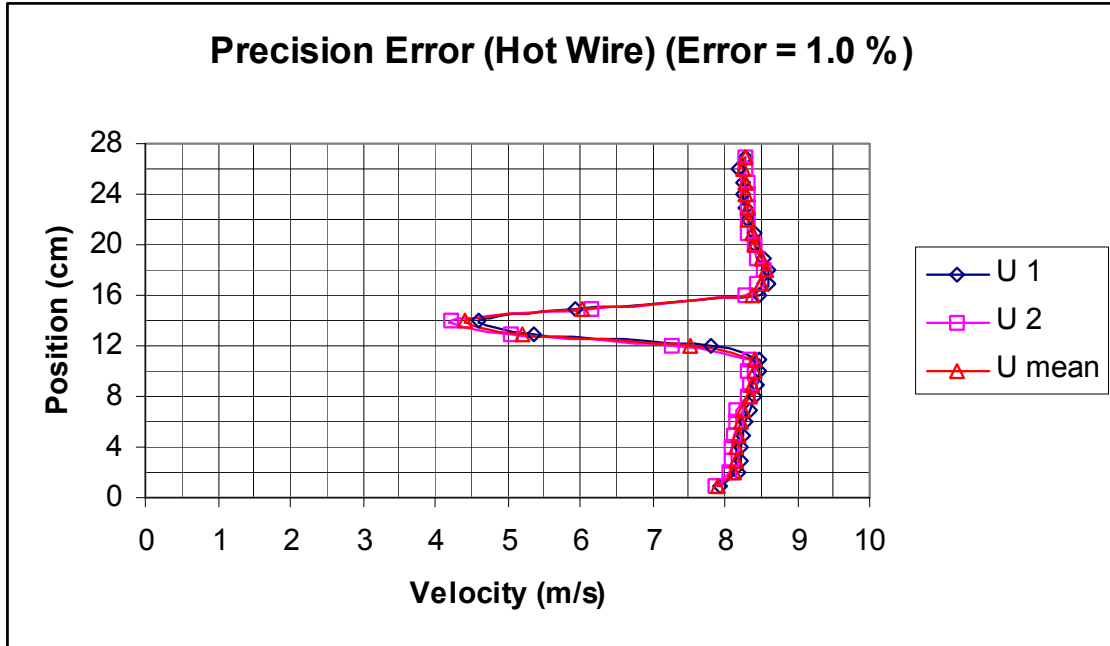


Figure C3. Hot Wire Precision Error

Clean Cylinder Error

The following error is in static probe readings of a clean cylinder. This was done to show the variations in data points using a variety of different probes.

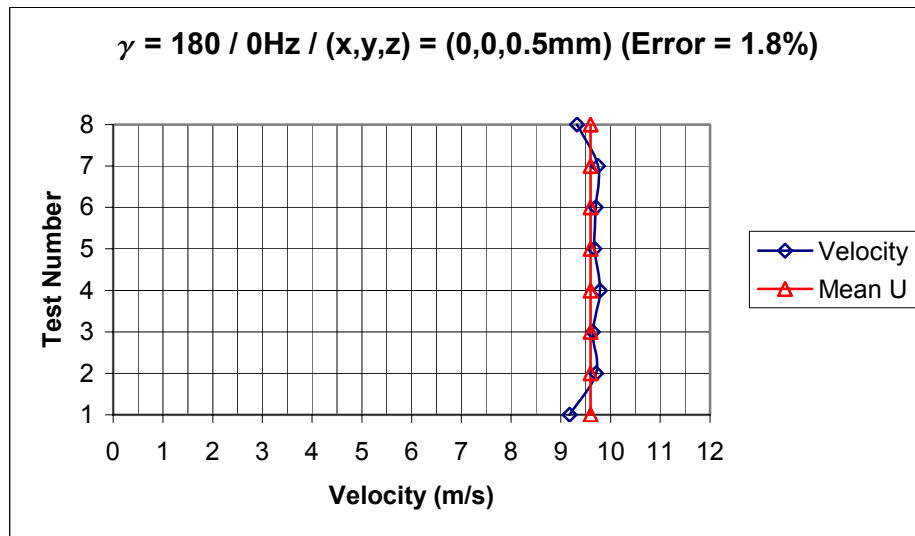


Figure C4. Clean Cylinder Static Point Error

Figure C4 shows data points taken with all three types of probes so an average 1.8 % precision error can be applied generally to the entire system.

Reference List

- (1) Cengel, Yunus A. and Boles, Michael A. Thermodynamics: An Engineering Approach (Third Edition). Massachusetts: WCB McGraw-Hill, 1998.
- (2) Gad-el-Hak, Mohamed and Bushnell, Dennis M. Separation Control: Review. Journal of Fluids Engineering, Volume 113/5. March 1991.
- (3) Huang A. and Folk, C. and Silva C. and Christensen, B. and Chen, Y. and Ho, C.M. and Jiang, F. and Grosjean, C. and Tai, Y.C. and Lee, G.B. and Chen, M. and Newbern, S. Application of MEMS Devices to Delta Wing Aircraft: From Concept Development to Transonic Flight Test. American Institute of Aeronautics and Astronautics, January 2001.
- (4) Incropera, Frank P. and DeWitt, David P. Fundamentals of Heat and Mass Transfer (Fourth Edition). New York: John Wiley and Sons, 1996.
- (5) Johnson, Gary W. LabVIEW Graphical Programming: Practical Applications in Instrumentation and Control. Massachusetts: McGraw Hill, 1994.
- (6) Johnston, James P. Pitched and Skewed Vortex Generator Jets for Control of Turbulent Boundary Layer Separation: A review. Third ASME/JSME Joint Fluids Engineering Conference. July 1999.
- (7) Khan, Zia U. and Johnston, James P. On Vortex Generating Jets. International journal of Heat and Fluid Flow, New York: Elsevier Science Inc, 2000.
- (8) Koester, David A. and Mahadevan, Ramaswamy and Hardy, Busbee and Markus, Karen W. MUMPS Design Handbook (Revision Seven). North Carolina: JDS Uniphase, MEMS Business Unit, 2001)
- (9) National Instruments Inc. AT-MIO/AI E series User Manual. Texas: Published by Author, May 1996.
- (10) River, R. B. and Sondergaard, R. and Bons, J. P. and Lake, J. P. Passive and Active Control of Separation in Gas Turbines. American Institute of Aeronautics and Astronautics, June 2000.
- (11) TSI Incorporated. Innovation in Thermal Anemometry. Minnesota: Published by Author
- (12) Wheeler, Anthony J. and Ganji, Ahmad R. Introduction to Engineering Experimentation. New Jersey: Prentice Hall, 1996.
- (13) White, Frank M. Viscous Fluid Flow (Second edition). Massachusetts: McGraw Hill, 1991.

Vita

Captain David M. Borgeson graduated from Hillwood High School in Nashville, Tennessee. He entered undergraduate studies at the Tennessee State University in Nashville, Tennessee where he graduated with a Bachelor of Science degree in Aeronautical Technology in August 1996. He was commissioned as a Second Lieutenant, USAF through the Detachment 790 AFROTC at the Tennessee State University in August 1996.

His first assignment was to Vandenberg AFB, California as an Undergraduate Space and Missile Training (USMT) student. In May 1997, he was assigned to the 30th Range Squadron, Vandenberg AFB, California where he served as a Range Control Officer and Range Operations Commander. He was then assigned to the 30th Operations Support Squadron as Chief, Range Operations Training at Vandenberg AFB, California. In August 2000, he entered the Graduate School of Engineering and Management, Air Force Institute of Technology. Upon graduation, he will be assigned to the 533rd Training Squadron, Det 1, Schriber AFB, Colorado.

REPORT DOCUMENTATION PAGE				Form Approved OMB No. 074-0188	
<p>The public reporting burden for this collection of information is estimated to average 1 hour per response, including the time for reviewing instructions, searching existing data sources, gathering and maintaining the data needed, and completing and reviewing the collection of information. Send comments regarding this burden estimate or any other aspect of the collection of information, including suggestions for reducing this burden to Department of Defense, Washington Headquarters Services, Directorate for Information Operations and Reports (0704-0188), 1215 Jefferson Davis Highway, Suite 1204, Arlington, VA 22202-4302. Respondents should be aware that notwithstanding any other provision of law, no person shall be subject to a penalty for failing to comply with a collection of information if it does not display a currently valid OMB control number.</p> <p>PLEASE DO NOT RETURN YOUR FORM TO THE ABOVE ADDRESS.</p>					
1. REPORT DATE (DD-MM-YYYY) 26-03-2002		2. REPORT TYPE MASTERS THESIS		3. DATES COVERED (From – To) SEP 2000 – MAR 2002	
4. TITLE AND SUBTITLE BOUNDARY LAYER CONTROL USING MICRO-ELECTROMECHANICAL SYSTEMS (MEMS)				5a. CONTRACT NUMBER	
				5b. GRANT NUMBER	
				5c. PROGRAM ELEMENT NUMBER	
6. AUTHOR(S) DAVID BORGESON, CAPT, USAF				5d. PROJECT NUMBER	
				5e. TASK NUMBER	
				5f. WORK UNIT NUMBER	
7. PERFORMING ORGANIZATION NAMES(S) AND ADDRESS(S) Air Force Institute of Technology Graduate School of Engineering and Management (AFIT/ENY) 2950 P Street, Building 640 WPAFB OH 45433-7765				8. PERFORMING ORGANIZATION REPORT NUMBER AFIT/GSO/ENY/02-1	
9. SPONSORING/MONITORING AGENCY NAME(S) AND ADDRESS(ES) D r . R i c h a r d R i v i r 1950 Fifth Street WPAFB, OH. 45433-7251				10. SPONSOR/MONITOR'S ACRONYM(S)	
				11. SPONSOR/MONITOR'S REPORT NUMBER(S)	
12. DISTRIBUTION/AVAILABILITY STATEMENT APPROVED FOR PUBLIC RELEASE; DISTRIBUTION UNLIMITED.					
13. SUPPLEMENTARY NOTES					
14. ABSTRACT <p>This study investigated the use of MEMS devices to control the boundary layer separation from a circular cylinder in cross flow. Velocity profiles were measured experimentally in a low speed wind tunnel. Momentum thickness was measured as the primary way to determine a change in the flow field. The goal was to determine the angular location and frequency of operation that would provide an effect on the boundary layer of the cylinder. A 25% reduction of momentum loss in the cylinder wake was detected with an optimal angle of 69 degrees and an optimal frequency of operation equal to that of the shedding frequency of the cylinder.</p>					
15. SUBJECT TERMS Boundary Layer, Micro-ElectroMechanical Systems, Momentum Thickness					
16. SECURITY CLASSIFICATION OF: UNCLASSIFIED			17. LIMITATION OF ABSTRACT UU	18. NUMBER OF PAGES 92	19a. NAME OF RESPONSIBLE PERSON Milton E. Franke
a. REPORT U	b. ABSTRACT U	c. THIS PAGE U			19b. TELEPHONE NUMBER (Include area code) (937) 785-6565, ext. 4720